AGU PUBLICATIONS

JGR

Journal of Geophysical Research: Solid Earth

RESEARCH ARTICLE
10.1002/2015JB011938

Key Points:
- First deep-water slip rate estimate for the Palos Verdes Fault (1.6–1.9 mm/yr)
- Holocene deformation is characterized by steeply dipping strike-slip faulting
- At least three Holocene earthquakes

Supporting Information:
- Figure S1 and Data Set S1
- Data Set S1

Correspondence to:
D. S. Brothers,
dbrothers@usgs.gov

Citation:
Brothers, D. S., J. E. Conrad, K. L. Maier, C. K. Paull, M. McGann, and D. W. Caress (2015), The Palos Verdes Fault offshore Southern California: Late Pleistocene to present tectonic geomorphology, seascape evolution, and slip rate estimate based on AUV and ROV surveys, *J. Geophys. Res. Solid Earth*, *120*, 4734–4758, doi:10.1002/2015JB011938.

Received 6 FEB 2015
Accepted 22 JUN 2015
Accepted article online 25 JUN 2015
Published online 30 JUL 2015

The Palos Verdes Fault offshore Southern California: Late Pleistocene to present tectonic geomorphology, seascape evolution, and slip rate estimate based on AUV and ROV surveys

Daniel S. Brothers[1], James E. Conrad[1], Katherine L. Maier[1], Charles K. Paull[2], Mary McGann[3], and David W. Caress[2]

[1]Pacific Coastal and Marine Science Center, U.S. Geological Survey, Santa Cruz, California, USA, [2]Monterey Bay Aquarium Research Institute, Moss Landing, California, USA, [3]Pacific Coastal and Marine Science Center, U.S. Geological Survey, Menlo Park, California, USA

Abstract The Palos Verdes Fault (PVF) is one of few active faults in Southern California that crosses the shoreline and can be studied using both terrestrial and subaqueous methodologies. To characterize the near-seafloor fault morphology, tectonic influences on continental slope sedimentary processes and late Pleistocene to present slip rate, a grid of high-resolution multibeam bathymetric data, and chirp subbottom profiles were acquired with an autonomous underwater vehicle (AUV) along the main trace of PVF in water depths between 250 and 600 m. Radiocarbon dates were obtained from vibracores collected using a remotely operated vehicle (ROV) and ship-based gravity cores. The PVF is expressed as a well-defined seafloor lineation marked by subtle along-strike bends. Right-stepping transtensional bends exert first-order control on sediment flow dynamics and the spatial distribution of Holocene depocenters; deformed strata within a small pull-apart basin record punctuated growth faulting associated with at least three Holocene surface ruptures. An upper (shallower) landslide scarp, a buried sedimentary mound, and a deeper scarp have been right-laterally offset across the PVF by 55 ± 5, 52 ± 4, and 39 ± 8 m, respectively. The ages of the upper scarp and buried mound are approximately 31 ka; the age of the deeper scarp is bracketed to 17–24 ka. These three piercing points bracket the late Pleistocene to present slip rate to 1.3–2.8 mm/yr and provide a best estimate of 1.6–1.9 mm/yr. The deformation observed along the PVF is characteristic of strike-slip faulting and accounts for 20–30% of the total right-lateral slip budget accommodated offshore Southern California.

1. Introduction

A significant challenge for paleoseismology is obtaining primary, near-field evidence for coseismic offset with accurate age constraints. For subaqueous studies, high-resolution marine geophysical methods are capable of imaging vertically offset stratigraphy and evidence for punctuated fault growth [*Barnes and Pondard*, 2010; *Bartholomew et al.*, 2014; *Brothers et al.*, 2009, 2011; *Pondard and Barnes*, 2010], as well as offset seabed/lakefloor morphology that can be dated to constrain late Pleistocene and Holocene slip rates [*Dingler et al.*, 2009; *Johnson et al.*, 2014; *Kent et al.*, 2005; *Ryan et al.*, 2012]. However, stratigraphic evidence for recent displacement along strike-slip faults is difficult to resolve in deep-water settings (>200 m) and two-dimensional cross sections are most practical for imaging vertical displacement. Other marine paleoseismic studies rely on secondary evidence to infer the timing of past events, such as seismoturbidite records [e.g., *Goldfinger*, 2011, and references therein], but turbidite emplacement is a nonunique process that can be difficult to link with a particular causative source [e.g., *Atwater et al.*, 2014; *Sumner et al.*, 2013]. Additionally, dating of event beds and offset geomorphic features requires high-precision coring, which is arduous in deep-water environments. There is a clear need to develop new approaches that can provide information on the kinematics, slip rates, and earthquake recurrence intervals for individual fault systems.

The Palos Verdes Fault (PVF) is part of a complex structural regime located offshore Southern California and referred to as the Inner Continental Borderland (ICB). Collectively, faults in the ICB played a central role in the North America-Pacific plate boundary evolution since ~30 Ma, including the transformation from Farallon Plate subduction along the former convergent margin to the formation of today's transform margin along the San Andreas Fault System [*Atwater and Stock*, 1998; *Bohannon and Geist*, 1998; *Crouch and Suppe*, 1993;

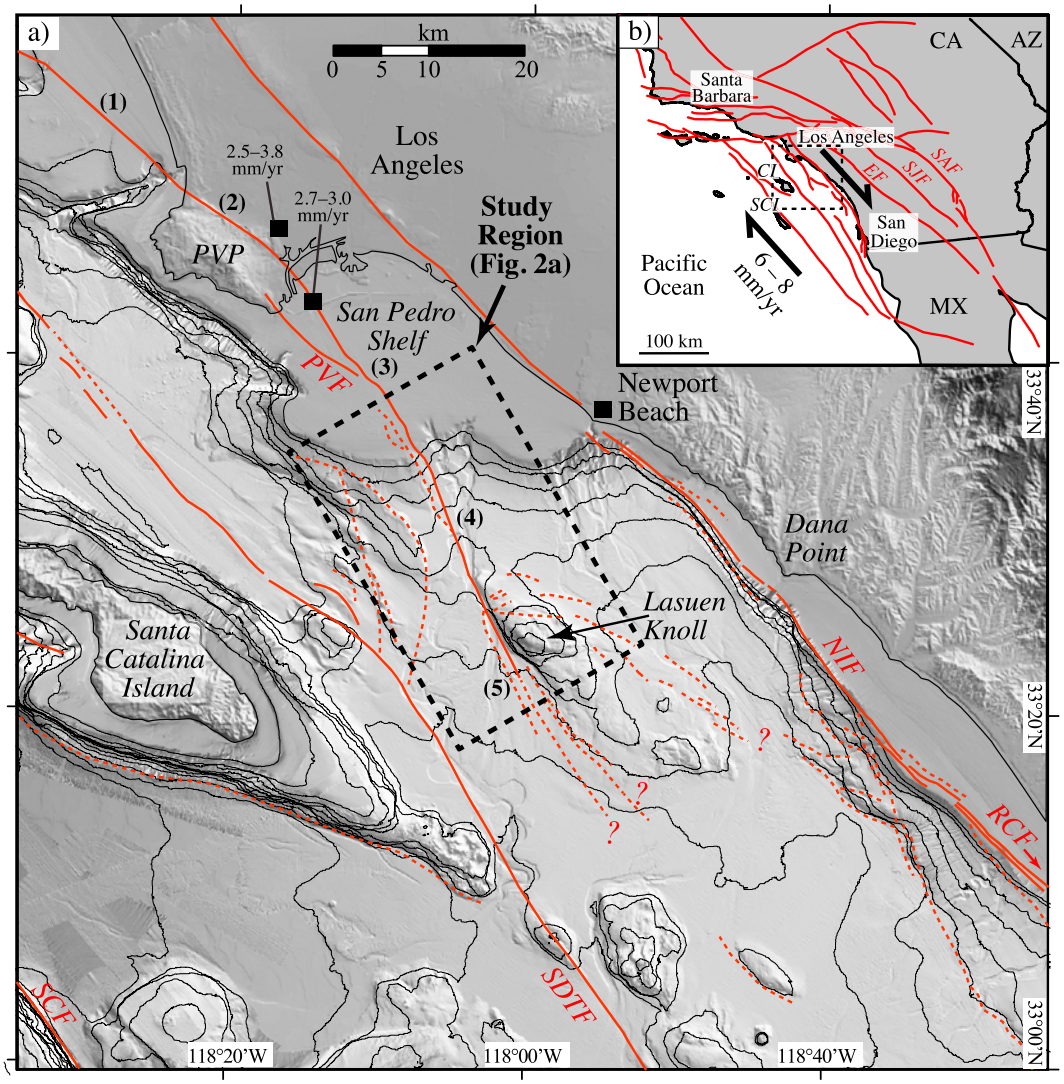

Figure 1. (a) Mosaic of shaded relief bathymetry [*Dartnell et al.*, 2014, 2015; *Gardner and Dartnell*, 2002; *NOAA*, 2014] and known active faults within the study region (solid red lines) [after *Dartnell et al.*, 2014; *Ryan et al.*, 2009, and references therein] and faults that are potentially Quaternary active (dashed red lines). Abbreviations: Palos Verdes Peninsula (PVP), Palos Verdes Fault (PVF), Newport-Inglewood Fault (NIF), San Diego Trough Fault (SDTF), San Clemente Fault (SCF), and Rose Canyon Fault (RCF). Numbers along the Palos Verdes Fault represent distinct sections based on orientation and observed deformation (see text for details): (1) Santa Monica Bay, (2) Palos Verdes Hills, (3) San Pedro Shelf, (4) San Pedro Slope, and (5) Lasuen Knoll. Previous slip rate estimates along the southeastern side of the PVP are from *Stephenson et al.* [1995] and *McNeilan et al.* [1996]. (b) Southern California tectonic setting, including slip vectors showing relative motion between San Clemente Island (SCI) and the mainland (black arrows) [*Bennett et al.*, 1996; *Platt and Becker*, 2010]. Red lines are generalized faults throughout Southern California [*U.S. Geological Survey and California Geological Survey*, 2014] (dashed box is the extent of Figure 1a). Abbreviations (not listed above): San Jacinto Fault (SJF), Elsinore Fault (EF), Santa Catalina Island (CI), San Clemente Island (SCI), and Transverse Ranges thrust belt (TRTB).

Legg, 1991; *Nicholson et al.*, 1994; *ten Brink et al.*, 2000]. Geodetic studies suggest the ICB presently accommodates ~6–8 mm/yr of dextral shear, which represents roughly 10–15% of the total plate boundary slip budget across Southern California [*Bennett et al.*, 1996; *DeMets et al.*, 2010; *Platt and Becker*, 2010]. The majority of this motion is distributed across a series of northwest trending strike-slip faults, including the PVF, located between San Clemente Island and the mainland (Figure 1) [*Ryan et al.*, 2009; *Legg et al.*, 2007].

With a few exceptions [*Astiz and Shearer*, 2000; *Grant and Shearer*, 2004; *Lindvall and Rockwell*, 1995; *McNeilan et al.*, 1996; *Ryan et al.*, 2012], the ICB lacks reliable constraints on how present-day tectonic deformation is partitioned among individual fault systems, which presents a major challenge to earthquake hazard

assessments for Southern California. Most of the active structures are located in deep-water settings where traditional approaches to neotectonic studies, such as trenching, are extremely difficult or impossible to apply. In water depths beyond 200 m, shipboard geophysical surveys often cannot resolve geomorphic features associated with individual earthquakes (i.e., features smaller than 5 m), which may lead to misinterpretation of larger-scale morphology that may not be representative of the tectonic processes most active in the recent past.

The Palos Verdes Fault (PVF) is an active northwest-southeast trending right-lateral strike-slip fault that involves onshore and offshore sections, extending from northern Santa Monica Bay, across the Palos Verdes Peninsula, and offshore again across the San Pedro Shelf and Slope (Figure 1). Although the PVF is considered to be a significant seismic hazard to Southern California [*Fisher et al.*, 2004b; *McNeilan et al.*, 1996; *Stephenson et al.*, 1995], its mode of deformation, recent activity, and earthquake hazards associated with its offshore extension are poorly constrained. The goal of the present study is to document primary, near-field evidence, including direct geomorphic and stratigraphic observations for late Pleistocene-present displacement along an offshore section of PVF (e.g., surface scarps, offset seafloor features, and vertical growth faulting). To do this, we employed a suite of geophysical and geological tools, the most important being high-resolution autonomous underwater vehicle (AUV) mapping and high-precision remotely operated vehicle (ROV) sediment sampling. We present an integrated analysis of (i) high-resolution multibeam bathymetry and subbottom chirp data acquired by an AUV operated by the Monterey Bay Aquarium Research Institute (MBARI), (ii) radiocarbon samples and deposits in vibracores collected by MBARI's ROV *Doc Ricketts* and U.S. Geological Survey (USGS) shipboard gravity cores, and (iii) seismic reflection profiles collected by the USGS and the exploration industry. Our results provide new constraints on continental slope sedimentary processes and on the fine-scale structure, kinematics, and slip rate of the PVF between the seaward edge of the San Pedro Shelf and Lasuen Knoll (Figures 1 and 2).

2. Background

The dominant mode of tectonic deformation in the ICB appears to be strike slip but remains poorly understood, in part, because few large earthquakes have occurred historically and prior studies have produced conflicting interpretations of fault kinematics [e.g., *Brankman and Shaw*, 2009; *Fisher et al.*, 2004a, 2004b; *Rivero et al.*, 2000; *Ryan et al.*, 2009; *Legg et al.*, 2007, 2015]. Nevertheless, at the latitude of Newport Beach, California, four steeply dipping, right-lateral strike-slip fault systems appear to carry most of the tectonic motion distributed across the ICB (Figure 1): Newport-Inglewood Fault, Palos Verdes Fault, San Diego Trough Fault, and the San Clemente Fault. Along-strike bends and steps recognized on these faults have generated complex patterns of transpressional uplift and transtensional subsidence [*Legg et al.*, 2007; *Mann*, 2007]. *Ryan et al.* [2012] provided the first Holocene marine geological slip rate estimate for the San Diego Trough Fault (1.5 ± 0.3 mm/yr). The Rose Canyon Fault, considered to be the southern extension of the Newport-Inglewood Fault, carries 1–2 mm/yr [*Lindvall and Rockwell*, 1995]; however, a possible decrease in Newport-Inglewood Fault's slip rate farther north [*Grant et al.*, 1997], plus recent geophysical mapping offshore Dana Point [*Dartnell et al.*, 2014], suggests that a significant percentage of the Newport-Inglewood-Rose Canyon slip budget may be transferred westward, possibly toward the PVF. A well-dated late Quaternary slip rate estimate for the San Clemente Fault has not been established.

The PVF can be split into five sections along its ~100 km length (Figure 1): Santa Monica Bay, Palos Verdes Hills, San Pedro Shelf, San Pedro Slope, and Lasuen Knoll [*Brankman and Shaw*, 2009]. Previous estimates of right-lateral strike-slip offset, uplift rates, and primary mode of deformation along the PVF have varied. A number of authors [e.g., *Brankman and Shaw*, 2009; *Shaw and Suppe*, 1996; *Sorlien et al.*, 2013] argued that the offshore PVF is not a steeply dipping strike-slip fault but is instead a moderately dipping reverse-oblique fault. Other studies argued that the PVF is a Quaternary-aged, high-angle strike-slip fault with a highly variable dip and sense of vergence due to along-strike changes in fault orientation [*Bohannon and Geist*, 1998; *Fisher et al.*, 2004a, 2004b; *McNeilan et al.*, 1996; *Ward and Valensise*, 1994]. For example, the most prominent zone of vertical uplift along the PVF is associated with a major restraining bend on the southward dipping Palos Verdes Hills section, also where Quaternary uplift rates are estimated between 0.1 and 0.4 mm/yr [*Ponti*, 1989; *Ward and Valensise*, 1994].

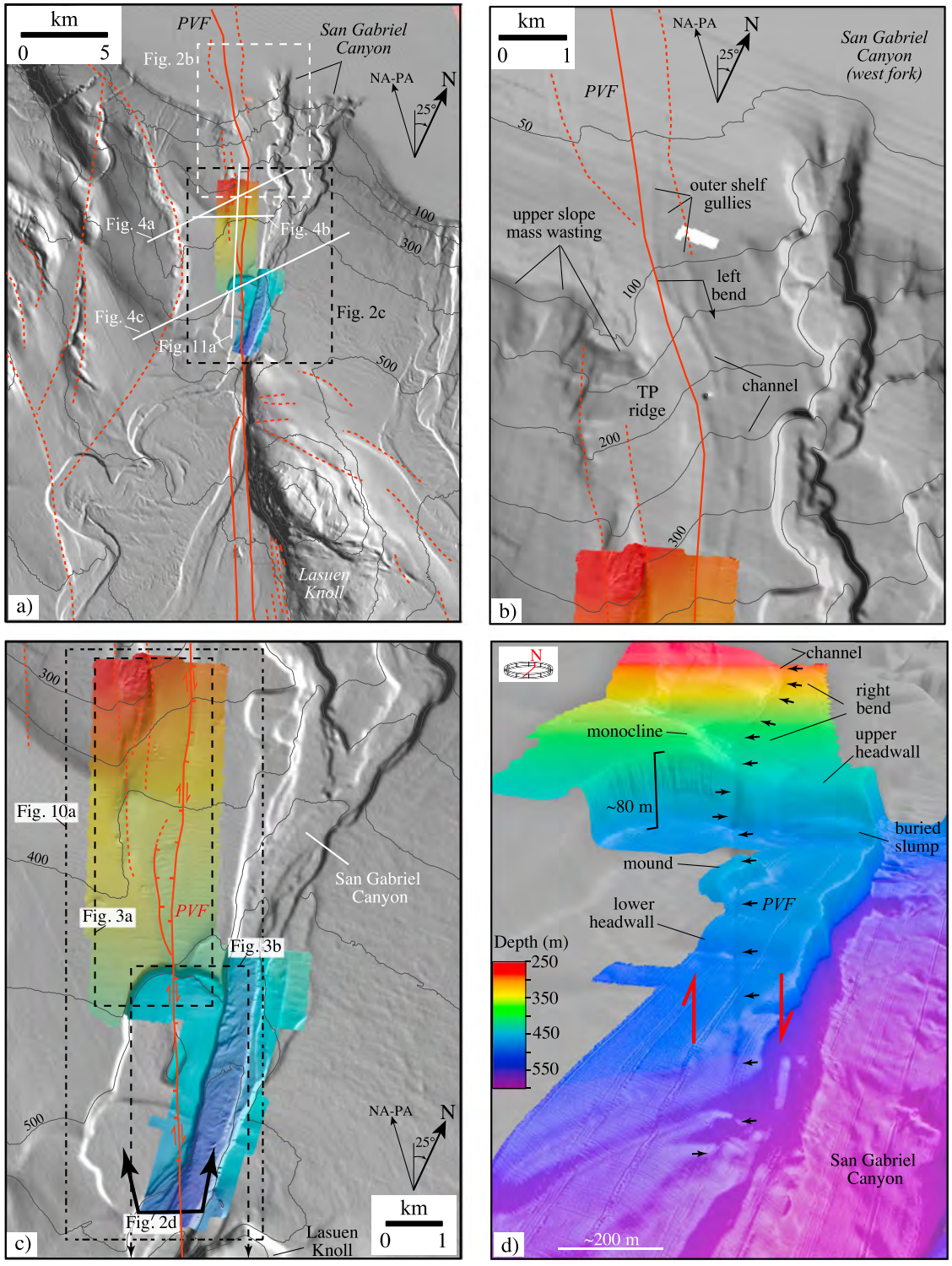

Figure 2. (a) Shaded relief bathymetry of the shelf edge and slope surrounding the Palos Verdes Fault (PVF). Dashed box based on 2 m resolution multibeam bathymetry collected by MBARI's autonomous underwater vehicle (enlarged in Figure 3c). Contours represent 100 m isobaths. The map frame is rotated to align with the trend of the PVF (~N25°W). Active faults are solid red lines; faults and/or folds that are potentially active are dashed [*Fisher et al.*, 2004a, 2004b, and references therein; *Marlow et al.*, 2000; this study]. (b) Enlarged section over the shelf edge and the west fork of the San Gabriel Canyon. Contours represent 50 m isobaths. (c) Color shaded relief of the 1 m resolution multibeam bathymetry data acquired during an autonomous underwater vehicle survey along the PVF and San Gabriel Canyon. Black arrows show direction of perspective view shown in Figure 3d. Dashed boxes show the extent of Figures 3a, 3b, and 10a. Core locations are shown in Figure 3. (d) Perspective view looking upslope along the primary trace of the PVF (denoted by black arrows). Important geomorphic features described in the text are labeled. A different color scale is used between plan views and perspective views.

Stephenson et al. [1995] estimated the late Quaternary (last 80–120 ka) right-lateral slip rate of the PVF to be 2.5–3.8 mm/yr based on channel deflections of the ancestral Los Angeles River (see Figure 1 study location). *McNeilan et al.* [1996] provided the first well-dated Holocene slip rate estimate for the PVF at 2.7–3.0 mm/yr and characterized recent motion along the PVF as high-angle, right-lateral strike slip. Although the thalwegs of buried, early Holocene stream channels imaged offshore Los Angeles Harbor (Figure 1) were determined to be right-laterally offset by 21–24 m, the subsurface mapping revealed a meandering channel system crossing relatively complicated near-surface fault structure, and sources of uncertainty in the slip rate estimates were not discussed in detail. Both *McNeilan et al.* [1996] and *Fischer et al.* [1987] estimated an average uplift rate of 0.3–0.4 mm/yr along the San Pedro Shelf section of the PVF.

Deep-penetration multichannel seismic reflection profiles reveal that the San Pedro Shelf section of the PVF separates heavily deformed Miocene and Pliocene strata on the western limb from relatively flat-lying upper Pliocene and Quaternary strata on the east, giving an up-to-the-southwest sense of offset [*Brankman and Shaw*, 2009; *Fischer et al.*, 1987, 2004b]. The orientation of this section (~N35°W) is slightly oblique to relative plate motion (N40°W; *Demets et al.* [2010]). The fault is nearly vertical in the upper 1 km but dips slightly westward farther down section [e.g., *Brankman and Shaw*, 2009; *Fisher et al.*, 2004a, 2004b]. Below ~3 km depth, however, the fault is poorly imaged in the seismic reflection data and Quaternary strata along the western limb of the fault are highly condensed or missing entirely [*Fischer et al.*, 1987].

Near the edge of the San Pedro Shelf, the degree of compressional folding decreases as the PVF bends to the southwest [*Fisher et al.*, 2004b]. The fault strikes ~N25°W for the entire length of the San Pedro Slope section and the northern 9 km of the Lasuen Knoll section (Figures 1 and 2). *Fisher et al.* [2004a, 2004b] noted evidence for transtension and normal faulting along the continental slope section of the fault. Strata along the shelf edge and upper slope are tilted toward San Gabriel Canyon, and the western edge of the canyon appears to follow the trend of the PVF from the shelf edge down to a water depth of ~600 m (Figures 1 and 2) [*Fisher et al.*, 2004b; *Marlow et al.*, 2000; *Normark et al.*, 2004].

Changes in fault dip and sense of motion near the base of the slope mark the transition between the San Pedro Slope and Lasuen Knoll sections [*Brankman and Shaw*, 2009; *Fisher et al.*, 2004b]. The PVF dips to the east along the western edge of Lasuen Knoll and exhibits up-to-the-northeast displacement [*Fisher et al.*, 2004b]. Previous studies identified seafloor scarps along these sections and proposed the fault has been active recently [*Marlow et al.*, 2000]. However, prior to the present study, constraints on the horizontal slip rate and paleoseismic history of the PVF seaward of the shelf edge did not exist due to the paucity of high-resolution marine geophysical data and high-precision geological sampling.

3. Data and Methods

In 2007 and 2008, a 24 km^2 patch of seafloor along the continental slope (250–600 m water depth) was mapped using the MBARI AUV to obtain ultrahigh-resolution multibeam bathymetry and subbottom chirp profiles. AUV navigation was obtained using a Kearfott inertial navigation system and a Doppler velocity log. The AUV carries a Reson 7100, 200 kHz multibeam sonar and an EdgeTech 2 to 16 kHz chirp subbottom profiler [*Caress et al.*, 2008]. The AUV was preprogrammed to proceed to >200 waypoints during each dive. Missions were up to 8.5 h in duration and were designed for the vehicle to fly at a speed of 3 knots while maintaining an altitude of 50 m above the seafloor. Track lines were oriented parallel to seabed contours and spaced at ~150 m to avoid holidays in swath coverage (e.g., Figure S1 in the supporting information). Resulting bathymetric elevation models were generated using 2 m horizontal grid size. Coincident with multibeam data collection, ~190 line km of chirp data was acquired, including several tie lines that span the AUV survey area. The chirp profiler can image stratigraphic horizons at a maximum vertical resolution of 0.11 m and a maximum subbottom depth of ~30 m. Seismic stratigraphy was mapped between profiles using *Kingdom Suite*, and fault displacement analysis was conducted using a combination of *Environmental Systems Research Institute ArcMap* and *International VLBI Service for Geodesy and Astronomy Fledermaus*. All subbottom depths and stratal thicknesses were estimated assuming 1500 m/s sound velocity.

Gravity cores and vibracores were collected along the PVF in an effort to sample and date sedimentary horizons showing evidence for coseismic deformation (Table 1, Figure 3, and Data Set S1). In 2009, aboard the R/V *Robert Gordon Sproul*, the USGS collected six gravity cores that ranged in length from 37 to

Table 1. Core Sample Locations and Basic Metrics

Core ID	Type of Core	Latitude	Longitude	Water Depth (m)	Length (cm)[a]
DR125 VC-85	vibracore	33.53391	−118.10371	362	166
DR125 VC-86	vibracore	33.53399	−118.10341	364	157
DR125 VC-87	vibracore	33.53406	−118.10365	365	172
DR125 VC-88	vibracore	33.53415	−118.10295	365	152
DR125 VC-89	vibracore	33.53428	−118.10256	366	154
DR125 VC-90	vibracore	33.53453	−118.10180	364	152
DR126 VC-91	vibracore	33.49513	−118.08938	495	168
DR126 VC-92	vibracore	33.49580	−118.08609	505	165
DR126 VC-93	vibracore	33.49755	−118.08823	443	144
DR135 VC-126	vibracore	33.53108	−118.11212	331	28
DR135 VC-127	vibracore	33.53128	−118.11138	331	33
DR135 VC-128	vibracore	33.53174	−118.10960	350	155
DR135 VC-129	vibracore	33.53380	−118.10398	421	166
DR135 VC-130	vibracore	33.53401	−118.10330	368	173
DR135 VC-131	vibracore	33.53435	−118.10223	372	171
DR136 VC-132	vibracore	33.50784	−118.09877	409	165
DR136 VC-133	vibracore	33.50820	−118.09701	419.7	174
DR136 VC-134	vibracore	33.50863	−118.09658	420	162
PV2-G1	gravity core	33.49338	−118.08722	508	161
PV4-G1	gravity core	33.50269	−118.08859	437	74
PV5-G1	gravity core	33.47144	−118.07188	520	44
PV6-G1	gravity core	33.46914	−118.07144	525	38
PV8-G1	gravity core	33.52834	−118.10244	375	89
PV9-G1	gravity core	33.52898	−118.10109	381	37

[a]The core lengths are corrected to reflect depth below the seafloor.

161 cm. In 2010, six dives of the MBARI *ROV Doc Ricketts* (DR125, 126, and 135–138) were conducted aboard the R/V *Western Flyer*. *ROV Doc Ricketts* was equipped with a vibracoring system and collected 18 vibracores that ranged in length from 28 to 172 cm. All cores were logged with a Geotek multisensor core logger, split, scanned with a GEOTEK digital line-scanning camera, and archived at the USGS in Menlo Park, California (see Data Set S1). Nine samples from two gravity cores and 34 samples from 13 vibracores were dated by accelerator mass spectrometry (AMS) ^{14}C at the National Ocean Sciences AMS (NOSAMS) facility at the Woods Hole Oceanographic Institution using primarily mixed planktic or mixed benthic foraminifera assemblages (Table 2). Two samples of terrestrial woody plant material and one marine mollusk shell sample (*Cyclocardia bailyi*) were also analyzed at NOSAMS. Marine carbonate samples were reservoir age corrected and calibrated. A 633 year reservoir age was used for the planktic foraminiferal samples [*Ingram and Southon*, 1996; *Stuiver and Braziunas*, 1993]. A 1750 year reservoir age was used for the benthic foraminifera and mollusk samples [*Mix et al.*, 1999]. The raw radiocarbon ages were then converted to calibrated ages using the CALIB 7.0.2 program [*Stuiver et al.*, 2014]. Calibrated ages and offset measurements are used to determine the fault slip rate.

In addition, the USGS conducted a series of ship-based geophysical surveys offshore Southern California (Figure S1), including high-resolution air gun multichannel seismic (MCS) reflection profiles, Huntec deep-towed seismic (DTS) reflection profiles [*Normark et al.*, 1999a, 1999b; *Sliter et al.*, 2005], SIG 2mille single-channel minisparker (500 J) seismic reflection profiles, and multibeam bathymetry [*Gardner and Dartnell*, 2002]. Seismic reflection data provide critical information on the fault geometry, deformation history, and regional tectonostratigraphic framework [e.g., *Fisher et al.*, 2004b]. High-resolution MCS data, single-channel seismic data, and Huntec DTS profiles were collected on a dense grid of track lines spaced at ~2–4 km over the shelf and slope of the study region (Figure S1). Ship-based multibeam bathymetry data along the San Pedro Shelf and Slope were acquired using a 300 kHz Kongsberg Simrad EM3000D system and a 30 kHz Kongsberg Simrad EM300 system [*Dartnell and Gardner*, 2009; *Gardner and Dartnell*, 2002]. Finally, several deep-penetration (>2 km) MCS profiles acquired by WesternGeco and Chevron between 1975 and 1985 were used to examine fault structure at depth (see http://walrus.wr.usgs.gov/NAMSS/).

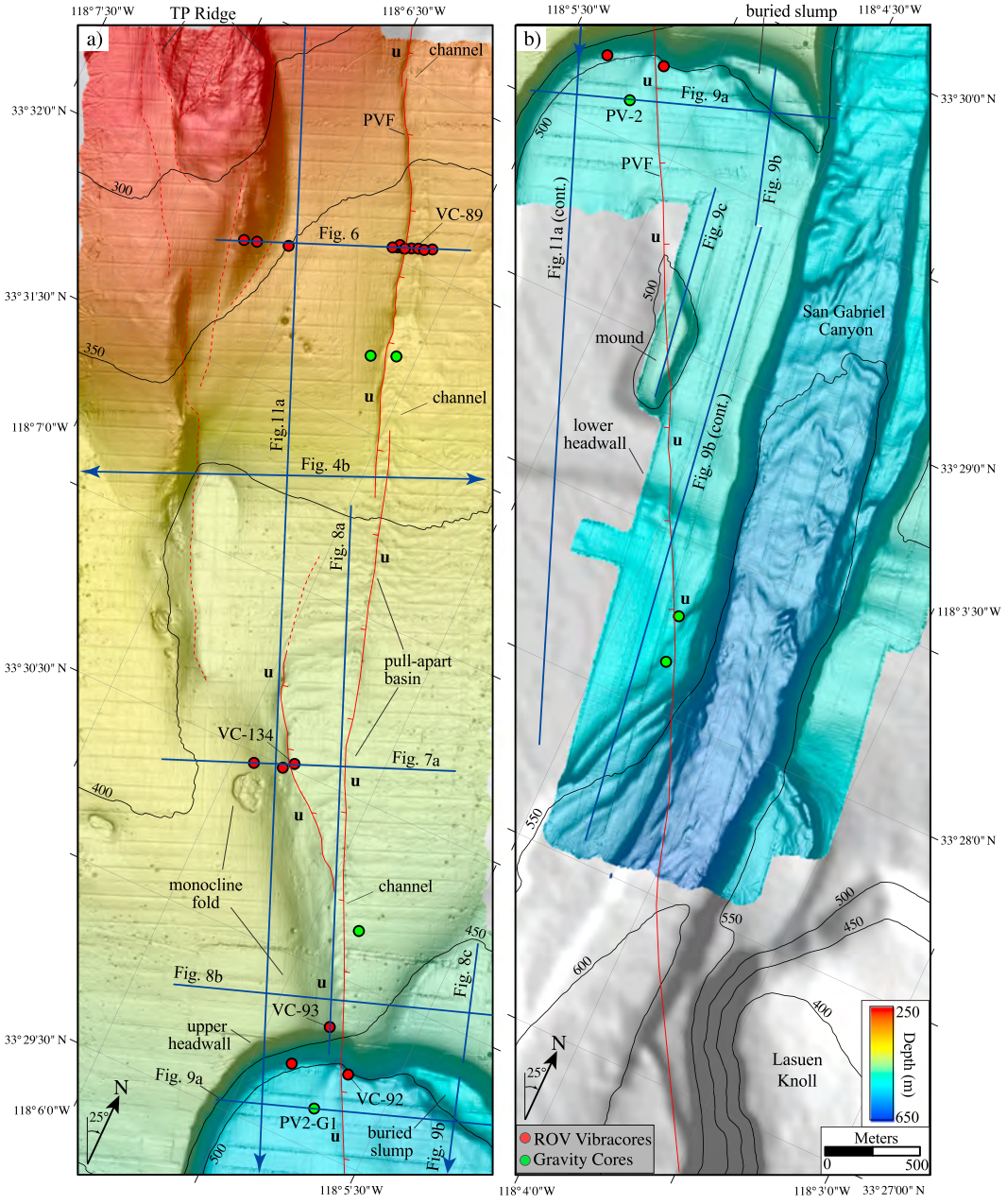

Figure 3. Colored shaded relief panels of 2 m resolution AUV bathymetry for (a) the upper section and (b) lower section of the survey area. Contours represent 50 m isobaths. Blue lines depict locations of select seismic reflection profiles. Relative vertical separation is labeled as "u" (upward motion) to highlight changes in the vertical separation along the PVF.

4. Results

4.1. Slope Morphology

The morphology of the San Pedro Shelf edge and Slope in the vicinity of the PVF (Figure 2) is characterized by the following: (1) submarine canyons, terraces, gullies, and deep-sea channels that run along the eastern limb of the PVF and then converge near the base of the slope with San Gabriel Canyon (Figure 2a) [*Dartnell and Gardner*, 2009]; (2) north-northwest trending ridges, troughs, and knolls associated with buried faults and folds [*Fisher et al.*, 2004b]; (3) a series of submarine landslide headwall and sidewall scarps with vertical relief ranging from 5 to 80 m (Figures 2b and 2c). The San Pedro Shelf edge is sinuous in plan view, weaving around the head of San Gabriel Canyon and smaller indentations

Table 2. Radiocarbon Dated Samples From Sediment Cores

Core ID	Depth Below Seafloor (cm)	Sample Type	δ13C	^{14}C Age (yr B.P.)	Age Error (±yr)	Calendar Age (cal yr B.P.)[a]	NOSAMS Accession #
DR125 VC-85	6–9	mixed planktic foraminifera	1.13	645	30	modern	OS-90856
DR125 VC-86	7–10	mixed planktic foraminifera	1.2	485	25	modern	OS-90860
DR125 VC-86	137–140	mixed planktic foraminifera	0.62	8,700	35	9,075	OS-90838
DR125 VC-87	7–10	mixed planktic foraminifera	1.09	200	30	modern	OS-90901
DR125 VC-87	72–75	mixed planktic foraminifera	1.45	5,450	30	5,582	OS-87139
DR125 VC-87	137–140	mixed planktic foraminifera	1.07	8,800	35	9,210	OS-90879
DR125 VC-89	6–9	mixed planktic foraminifera	1.28	705	35	84	OS-90898
DR125 VC-89	34–37	mixed planktic foraminifera	0.73	3,030	30	2,553	OS-87225
DR125 VC-89	44–45	plant material (wood)	−26.18	4,140	35	4,140	OS-94114
DR125 VC-89	54–57	mixed planktic foraminifera	1.43	5,660	35	5,803	OS-87704
DR125 VC-89	71–75	mixed planktic foraminifera	1.21	7,760	35	7,981	OS-87563
DR125 VC-89	136–139	mixed planktic foraminifera	0.76	10,350	40	11,128	OS-90877
DR125 VC-90	7–10	mixed planktic foraminifera	1.17	1,060	30	466	OS-90989
DR125 VC-90	72–76	mixed planktic foraminifera	1.63	6,230	25	6,408	OS-90878
DR126 VC-92	7–10	mixed planktic foraminifera	1.17	1,840	25	1,179	OS-90900
DR126 VC-92	72–75	mixed planktic foraminifera	0.93	4,480	30	4,355	OS-90880
DR126 VC-92	137–140	mixed planktic foraminifera	1.4	6,460	30	6,675	OS-90891
DR126 VC-93	6–9	mixed planktic foraminifera	0.81	7,760	25	7,979	OS-90881
DR126 VC-93	71–74	mixed benthic foraminifera	−0.24	21,200	70	23,424	OS-90882
DR126 VC-93	136–139	mixed planktic foraminifera	−1.01	27,400	120	30,937	OS-90896
DR135 VC-126	18–21	mixed benthic foraminifera	0.3	44,400	2100	46,086	OS-111535
DR135 VC-127	21–24	mixed planktic foraminifera	−1.13	24,400	100	27,822	OS-87562
DR135 VC-128	6–9	mixed planktic foraminifera	1.69	3,590	45	3,218	OS-91011
DR135 VC-128	71–74	mixed planktic foraminifera	0.73	9,900	50	10,563	OS-91016
DR135 VC-128	136–139	mixed planktic foraminifera	−0.04	12,700	60	13,949	OS-91044
DR135 VC-129	7–10	mixed planktic foraminifera	1.3	455	35	modern	OS-91013
DR135 VC-129	72–75	mixed planktic foraminifera	1.75	5,880	35	6,050	OS-91042
DR135 VC-129	137–140	mixed planktic foraminifera	1.28	8,940	40	9,386	OS-91040
DR135 VC-130	8–11	mixed planktic foraminifera	0.92	815	30	222	OS-91017
DR135 VC-130	73–76	mixed planktic foraminifera	1.37	5,690	35	5,833	OS-91037
DR135 VC-130	138–141	mixed planktic foraminifera	0.75	8,370	40	8,606	OS-91038
DR135 VC-131	6–9	mixed planktic foraminifera	2.02	480	30	modern	OS-91015
DR135 VC-131	71–74	mixed planktic foraminifera	1.45	7,710	40	7,937	OS-91008
DR135 VC-131	136–139	mixed planktic foraminifera	0.76	9,380	40	9,924	OS-91041
PV2-G1	5–7	mixed benthic foraminifera	−0.74	1,200	25	modern	OS-77407
PV2-G1	45–47	mixed benthic foraminifera	−0.89	2,710	30	908	OS-77408
PV2-G1	84–88	mixed benthic foraminifera	−2.09	4,260	50	2,691	OS-77409
PV2-G1	124	mollusk (*Cyclocardia bailyi*)	1.04	3,880	35	2,207	OS-77412
PV2-G1	128–130	mixed planktic foraminifera	1.47	4,220	30	3,992	OS-88363
PV2-G1	133.5–134.5	plant material (wood)	−27.61	3,690	30	3,690	OS-78006
PV2-G1	141–145	mixed benthic foraminifera	−0.84	10,450	50	9,830	OS-77410
PV2-G1	157–159	mixed planktic foraminifera	0.89	4,780	30	4,762	OS-88344
PV8-G1	20–22	mixed benthic foraminifera	−0.18	6,140	35	5,066	OS-77411

[a]Reservoir correction and calibration were performed using CALIB 7.0.2 [*Stuiver et al.*, 2014]. The core lengths are corrected to reflect depth below the seafloor.

to the west San Gabriel Canyon associated with gullies (Figures 2a and 2b). Below the shelf edge, San Gabriel Canyon is relatively straight and follows the trend of the PVF to the northwestern edge of Lasuen Knoll, where it splits into two channels on the seafloor; the eastern channel is bounded by Lasuen Knoll, whereas the western channel meanders along the basin floor [*Fisher et al.*, 2004b; *Marlow et al.*, 2000; *Normark et al.*, 2004].

Gullies and channels emanating from the shelf edge to the west of San Gabriel Canyon converge into a subtle channel that follows the trend of the PVF for a distance of ~10 km down to ~450 m water depth, where both the elongate channel and the PVF intersect a 1.7 km wide landslide headwall scarp (Figures 2 and 3). The channel is bounded to the west by a northwest trending transpressional ridge and to the east by the active trace of the PVF. Near the upslope extent of AUV data coverage, this channel is 150–170 m wide and 5–10 m deep (Figure 3a). Crescentic bedforms oriented perpendicular to the slope gradient occur in the

channel and seafloor immediately surrounding the fault trace (Figure 3a). They begin just below a change in slope gradient at ~370 m water depth, where the slope gradient decreases. Near the 400 m isobath, the channel width increases to ~500 m and then merges with a northwest trending monocline about 1 km above the headwall scarp ("upper headwall" here onward). Hundreds of circular and semicircular seabed depressions ranging from 5 to 200 m in diameter are observed above the upper headwall. The depressions appear to be pockmarks [*Judd and Hovland*, 2007] but show no obvious association with other geomorphic features beyond that they are not observed on the seafloor below the upper headwall (Figure 3b).

The fault is expressed as a narrow (100 m), linear trough as it crosses the upper headwall scarp. The steep scarp face (between 15° and 45°) has up to 80 m of relief (Figures 2d and 3). At the PVF, the upper headwall scarp is displaced right-laterally. West of the PVF, the upper headwall scarp curves smoothly southward, orthogonal to bathymetric contours, and becomes a continuous sidewall scarp for roughly 2 km before merging with a complex of headwall and sidewall scarps (Figures 2c, 2d, and 3). To the east of the PVF, the upper headwall curves upslope around a 10 m high, back-tilted step ("buried slump" in Figures 2d and 3) before intersecting the San Gabriel Channel.

Below the upper headwall, within the landslide evacuation zone, the seabed is relatively smooth and the fault trace is expressed as a subtle seafloor lineament. The fault continues on a N25°W orientation, cuts through a small (100 × 500 m) bathymetric mound and a second, lower headwall scarp, and then crosses the western bank of San Gabriel Canyon (Figure 3b). The fault has right-laterally offset the mound and lower headwall (Figures 2d and 3b). Terraces along the western margin of San Gabriel Canyon bend westward abruptly where they intersect the fault. However, there is no definitive expression of the PVF on the channel floor or along its projected path to the west of Lasuen Knoll (Figures 2a, 2c, and 3b).

4.2. Structure and Stratigraphy

Just below the shelf edge, the PVF takes a slight left bend, or restraining bend, and defines the eastern edge of a transpressional ridge (labeled "TP ridge" in Figure 2b). Along TP ridge, the fault is steeply dipping to the west (Figure 4) [*Fisher et al.*, 2004b]; near the toe of TP ridge, the fault displays a right bend, or releasing bend, where it splays and forms a small, lazy-z-type pull-apart basin (Figures 2c, 2d, and 3a) [term from *Mann et al.*, 1983] and then assumes a nearly constant strike of ~N25°W down to Lasuen Knoll. Uplifted and tightly folded strata underlie a monocline that converges with the active strands of the PVF just above the upper headwall. MCS profiles reveal evidence for faulting and growth folding beneath the monocline [e.g., *Fisher et al.*, 2004b], but the absence of seabed scarps, lineaments, or other evidence for recent displacement (Figures 2 and 3) suggests the deformation is no longer active. MCS and single-channel minisparker data also reveal that between the upper headwall and the southern limit of the AUV data coverage, the primary trace of the PVF is nearly vertically dipping to the basement interface (Figure 4).

The following sections describe key elements of the late Pleistocene-Holocene tectonic geomorphology and substrate geology needed to constrain the timing and style of deformation along the PVF. Descriptions start near the upslope extent of the AUV data coverage and progressively step downslope. The grid of high-resolution AUV chirp subbottom profiles was used to construct a three-dimensional late Pleistocene and Holocene chronostratigraphic framework for the study site. Radiocarbon samples from cores provided age control for stratigraphic marker beds imaged in subbottom data (Table 2). Representative core logs are shown in Figure 5, and the entire suite of core logs is provided in Data Set S1.

The shallow-type section in this study includes a slope perpendicular transect of 11 ROV vibracores, nine of which were radiocarbon dated and coincide with AUV chirp profile z20815 (Figures 3a and 6). The PVF is revealed by vertically offset strata imaged beneath a ~2 m seafloor scarp that coincides with the southwestern channel margin. On this profile, we do not observe evidence for increasing vertical throw with depth, or "fault growth", in the upper 10 m, but deeper strata diverge and thicken into the PVF. All layers imaged in the chirp data onlap and pinch out on the east flank of TP ridge. Dated samples from vibracores DR135 VC-126 and VC-127 (Table 2) confirm the younger units are missing along TP ridge and corroborate the age of deeper strata that are also sampled farther downslope and described later (i.e., the 31 ka and 23 ka horizons). The transect of vibracores penetrates up to 174 cm of predominantly fine-grained sediments and includes bioturbated mud with few turbidite beds containing very fine to medium-grained sand and woody organic material (Figures 5 and 6, and Data Set S1). Based on correlation with radiocarbon ages from the cores, the base of the

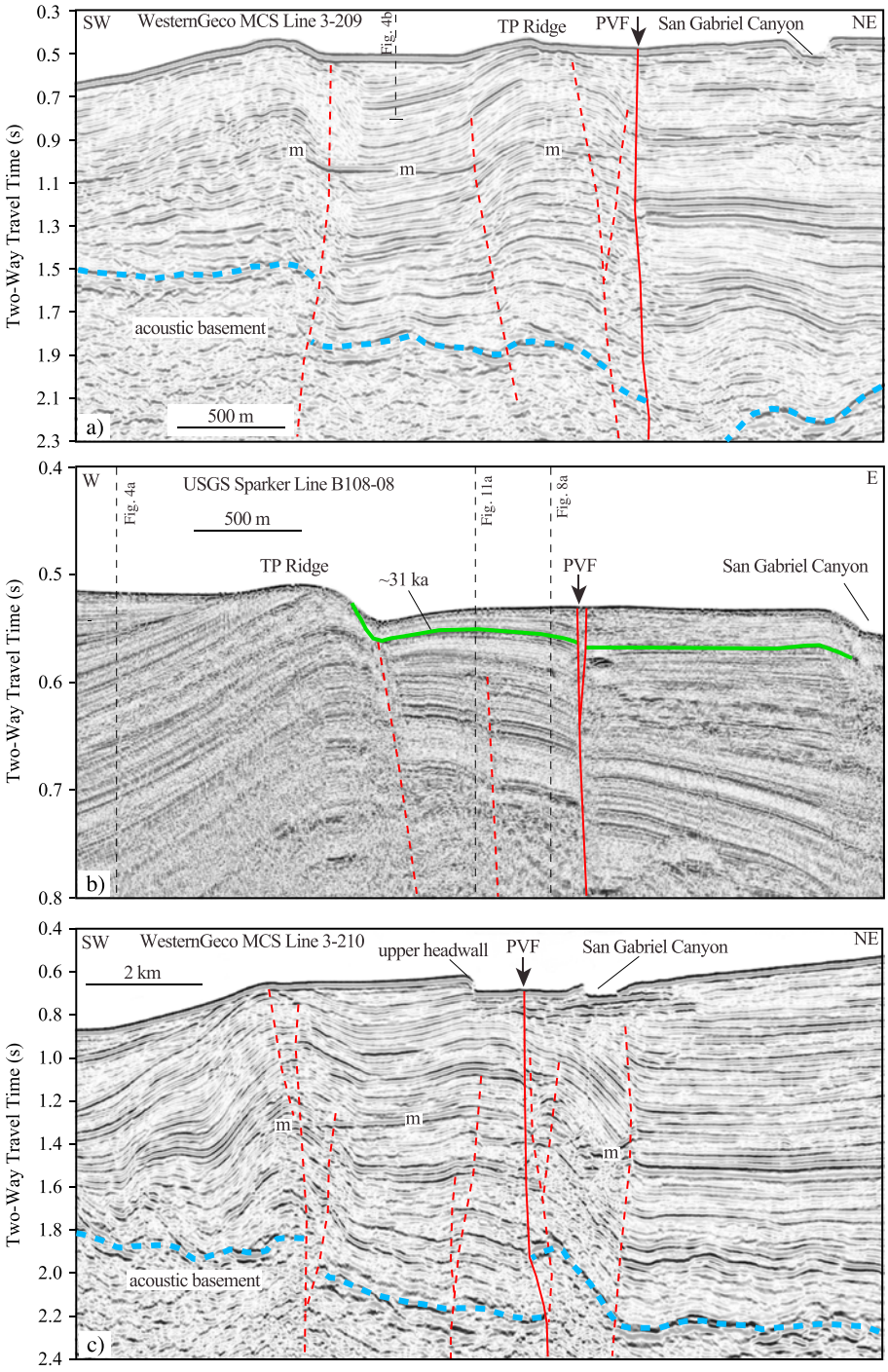

Figure 4. Seismic reflection profiles across the Palos Verdes Fault (PVF). Solid red lines are definitive fault locations; dashed lines are inferred faults and/or faults that appear to be inactive. (a) WesternGeco multichannel seismic reflection profile across the Palos Verdes Fault (PVF; see Figure 2a for location) adjacent to the transpressional ridge ("TP Ridge"). Note that the fault dip is nearly vertical and restricted to a single splay. (b) High-resolution single-channel sparker profile (see Figure 2c for location). The 31 ka horizon is based on a radiocarbon age from vibracore DR126 VC-93 (Figure 3a) and traced throughout the study area in subbottom profiles. (c) WesternGeco multichannel seismic reflection profile across the lower slope (see Figure 2a for location).

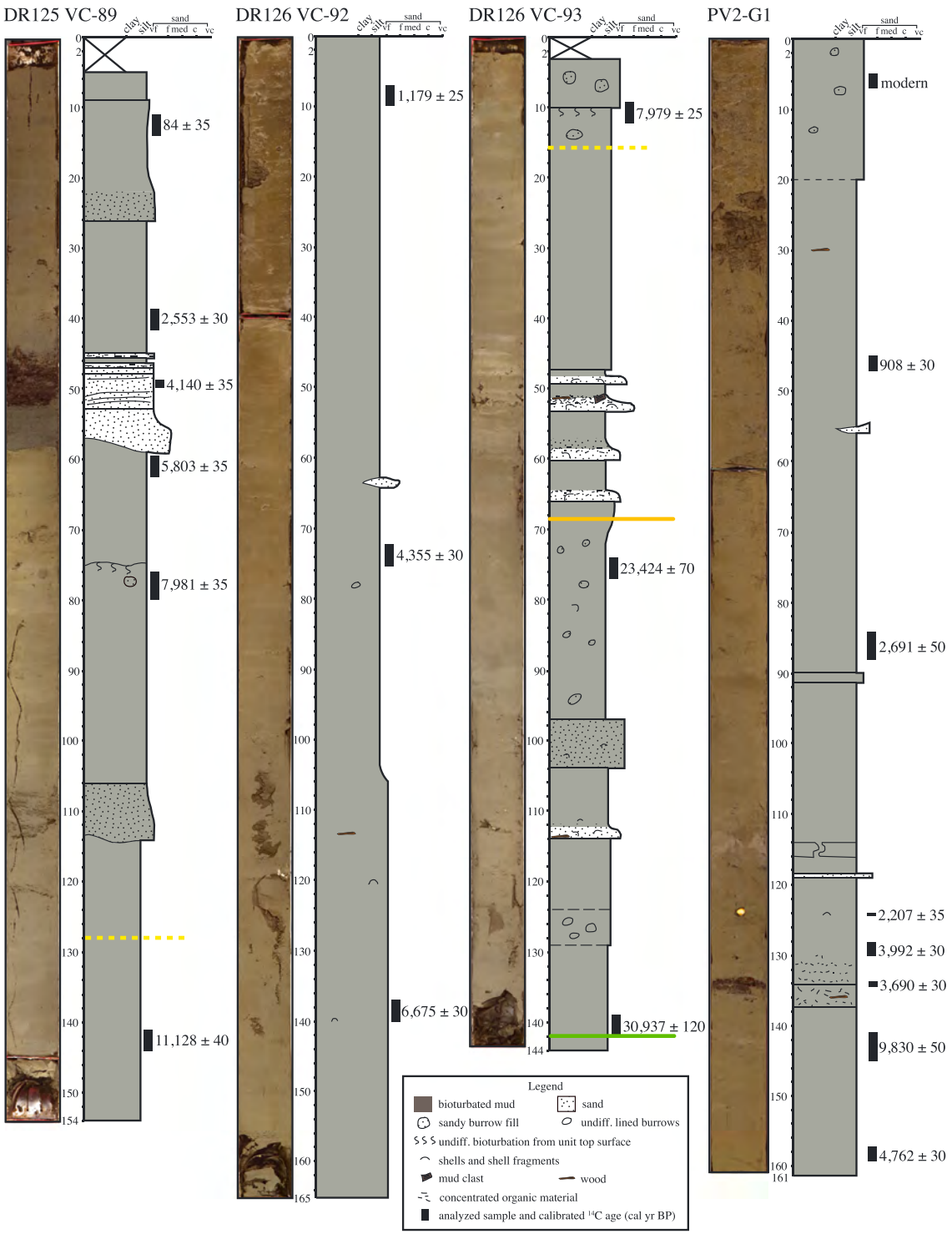

Figure 5. Core photographs and lithological logs of select sediment cores (see Table 1 and Data Set S1). Sample ages represent calibrated radiocarbon dates with analytical error (see Table 2). Overall sediment accumulation rates are greater for cores DR126 VC-92 and PV2-G1 located below the upper headwall (see Figure 3) than for DR126 VC-93 from above the upper headwall. Vibracore DR125 VC-89 from a channel next to the Palos Verdes Fault (see Figure 3) contains at least one sandy turbidite representative of a mid-Holocene event. Colored lines represent approximate locations of key marker horizons identified in AUV Chirp profiles: base of Holocene (dashed yellow), ~23 ka horizon (orange), and ~31 ka horizon (green).

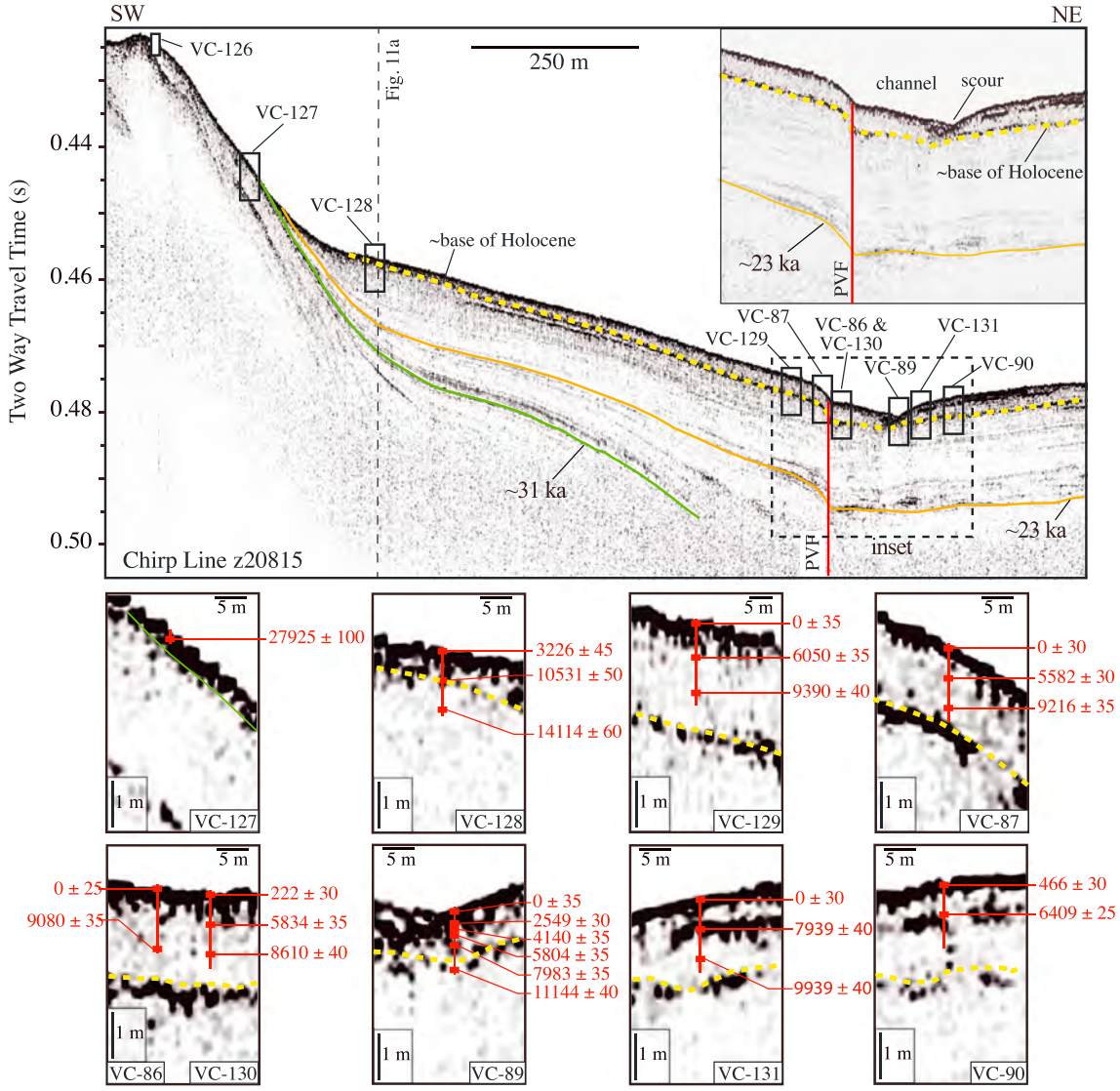

Figure 6. ROV vibracore transect with radiocarbon ages correlated with an AUV chirp profile (see Figure 3a for location). Enlarged sections reveal the associations between acoustic character and radiocarbon dates (see Table 2). Inset highlights evidence for scour (e.g., truncation and thinning) along the eastern edge of the seabed channel.

Holocene (~10 kyr B.P.) is correlated with a strong impedance boundary that separates high-amplitude, chaotic reflections above from lower-amplitude, continuous reflections below (Figure 6). The thickness of the Holocene sediment (~2 m) remains constant on either side of the PVF; however, the layer thins toward the northeastern channel margin, suggesting erosional scour in the channel has occurred during the Holocene. The seafloor bedforms noted above appear to be confined to the Holocene package.

Roughly 2 km downslope of the type section described above, the PVF takes a ~5° releasing bend and splits into two splays that bound a small pull-apart basin (Figures 2, 3a, and 7); the basin fill contains the only definitive stratigraphic evidence for multiple Holocene surface ruptures (see interpretations in section 5.2). Holocene strata appear to diverge and thicken toward the eastern splay of the PVF (Figure 7), and vertical offset increases from the seafloor to the basal Holocene reflector. Holocene sediment thickness varies considerably in and around the pull-apart basin (Figure 7). Bedforms observed farther upslope in and around the channel have greater amplitude (1.5–2.0 m) and wavelength (200–300 m) within the pull-apart basin. A dip profile crossing the basin (Figure 8a) shows a series of features that are common to upslope-migrating sediment waves [*Lee et al.*, 2002], including stacked, lenticular reflectors whose upslope flanks are thicker than the downslope flanks.

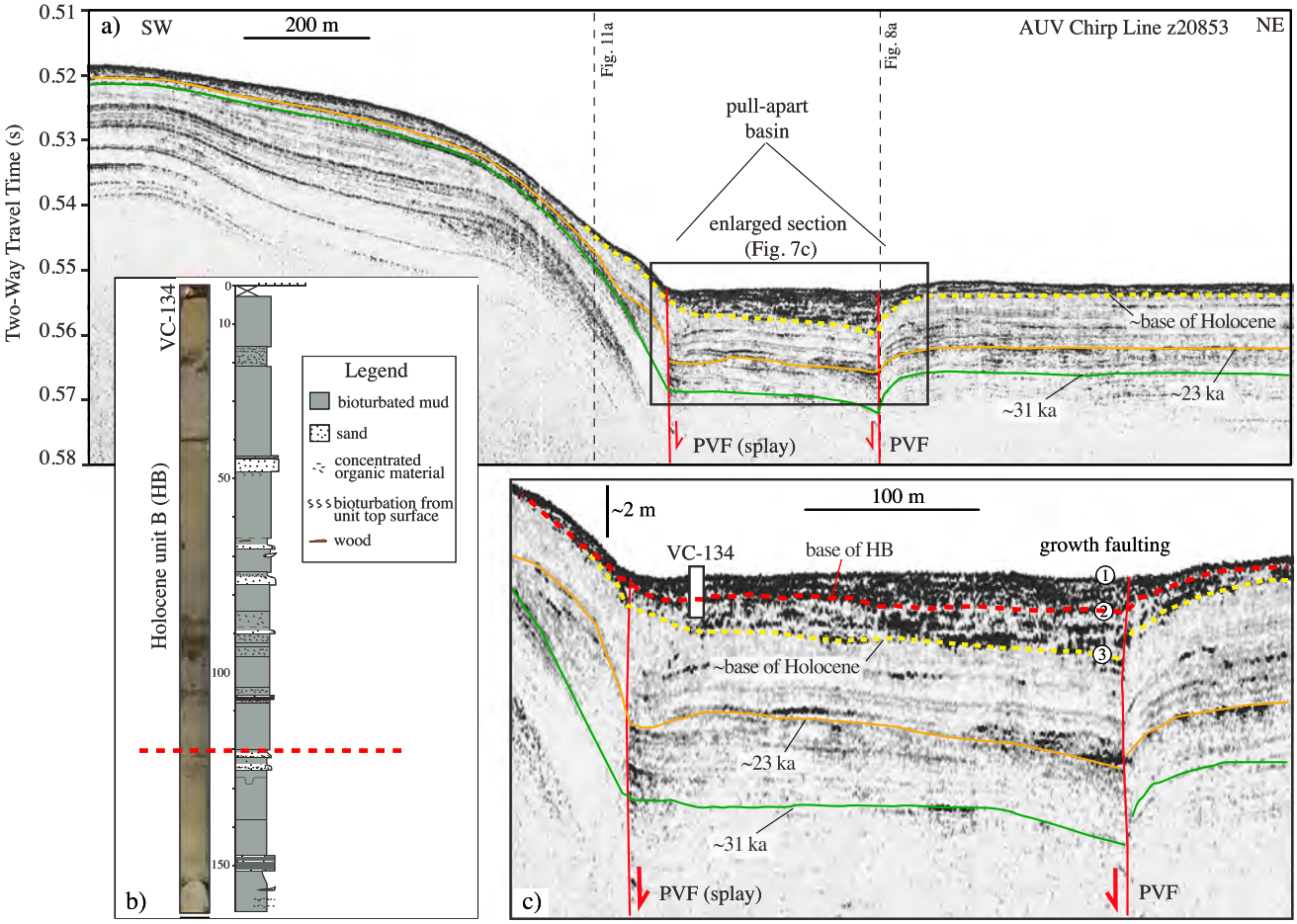

Figure 7. Cross section of the pull-apart basin (see Figure 3 for location). (a) AUV chirp profile highlighting the late Pleistocene and Holocene stratigraphy. (b) Vibracore DR136 VC-134 photograph, lithological log, and interpreted correlation with seismic horizon HB (dashed red line). This core contains many Holocene event beds in the pull-apart basin. (c) Enlarged section from Figure 7a highlighting evidence for punctuated Holocene vertical growth faulting and marked stratigraphic thickening and divergence into the eastern splay of the PVF (numbers indicate punctuated increases in vertical offset with depth).

South of the pull-apart basin, the splay faults converge onto a single fault, which then intersects the upper headwall (Figure 3a). Along the single fault strand, the PVF offsets shallow strata and displays up-to-the-east displacement superimposed on the limb of a broad monocline fold (Figure 8b). Vibracore DR126 VC-93 (Figures 3a and 5 and Data Set S1), located on the edge of the upper headwall scarp, confirms that the Holocene deposits correspond to the package of high-amplitude reflectors observed throughout the survey area and nearly pinch out proximal to the upper headwall (Figures 8a and 8c). Samples from DR126 VC-93 also provided age control for the bases of two late Pleistocene marker beds (~31 ka and 23 ka) that were traced upslope throughout the survey area. Both of these layers show evidence for thinning and downlap toward the headwall scarp, whereas underlying older horizons are either concordant or display marked thickening into the scarp face (Figures 8a and 8c). This variation in stratal geometry provides an important constraint on the age of the upper headwall, as discussed later in section 5.1.

The substrate character and deposition rates change dramatically at the base of the upper headwall. The direction of vertical throw on the PVF changes along strike (Figures 3b, 9a, and 9c). North of the bathymetric mound, the fault is characterized by down-to-the-east displacement and ~2 m of growth faulting within the visible section (Figures 3b and 9a). The sense of vertical offset is unclear beneath the mound (Figure 9c) but is up to the northeast to the south of the mound (Figure 3b). Gravity core PV2-G1 bottoms out at 161 cm in massive bioturbated mud dated to ~4.8 kyr B.P., and ROV vibracore DR126 VC-92 recovered 165 cm of massive bioturbated mud dated to ~6.7 kyr B.P. at 137–140 cm (Table 2 and Figure 5).

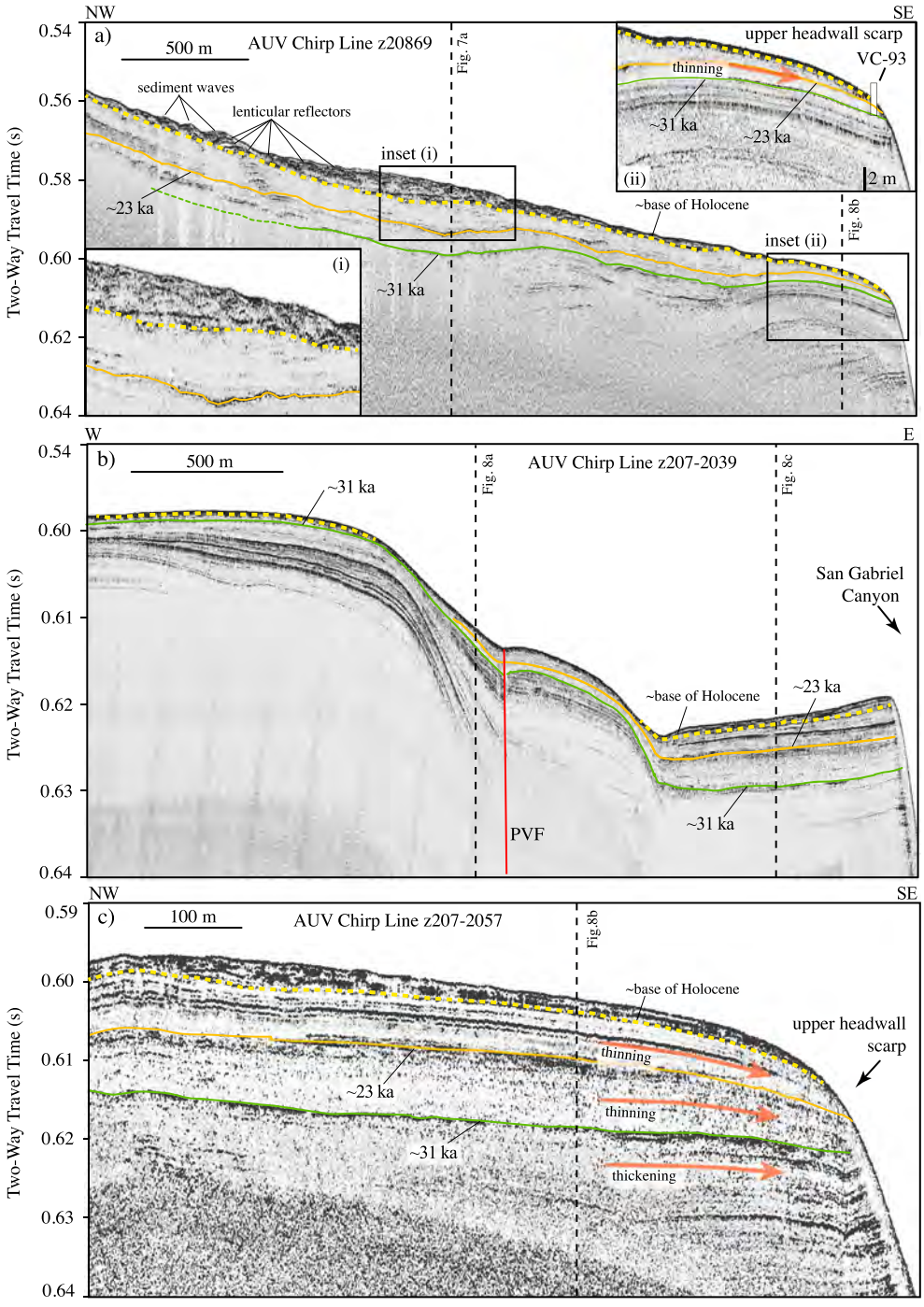

Figure 8. Panel of AUV chirp profiles near the upper headwall scarp. (a) Dip line crossing the fault-bounded channel, the pull-apart basin, and the upper headwall. Enlarged inset (i) shows buried sediment waves within the pull-apart basin. Enlarged inset (ii) illustrates the correlation of core DR126 VC-93 (see Figure 5) with subbottom data, as well as ages and geometries of subsurface sediment packages. The bottom of DR126 VC-93 sampled the top of a ~31 ka marker horizon (green line; see Figure 5). (b) Strike line crossing the PVF. (c) Dip line across the upper headwall. Note layers above the red horizon thin scarpward in both this line and in Figure 8a.

The ~10 kyr B.P. age from 141 to 145 cm in PV2-G1 is disregarded as it is likely to be older, reworked material (Table 2 and Figure 5). By extrapolating the average sedimentation rates calculated from the base of PV2-G1 (~34 cm/kyr) and the deepest sample in DR126 VC-92 (~20 cm/kyr), the base of the Holocene section at both core sites appears to coincide with a relatively strong impedance boundary (e.g., Figure 9a). Most chirp

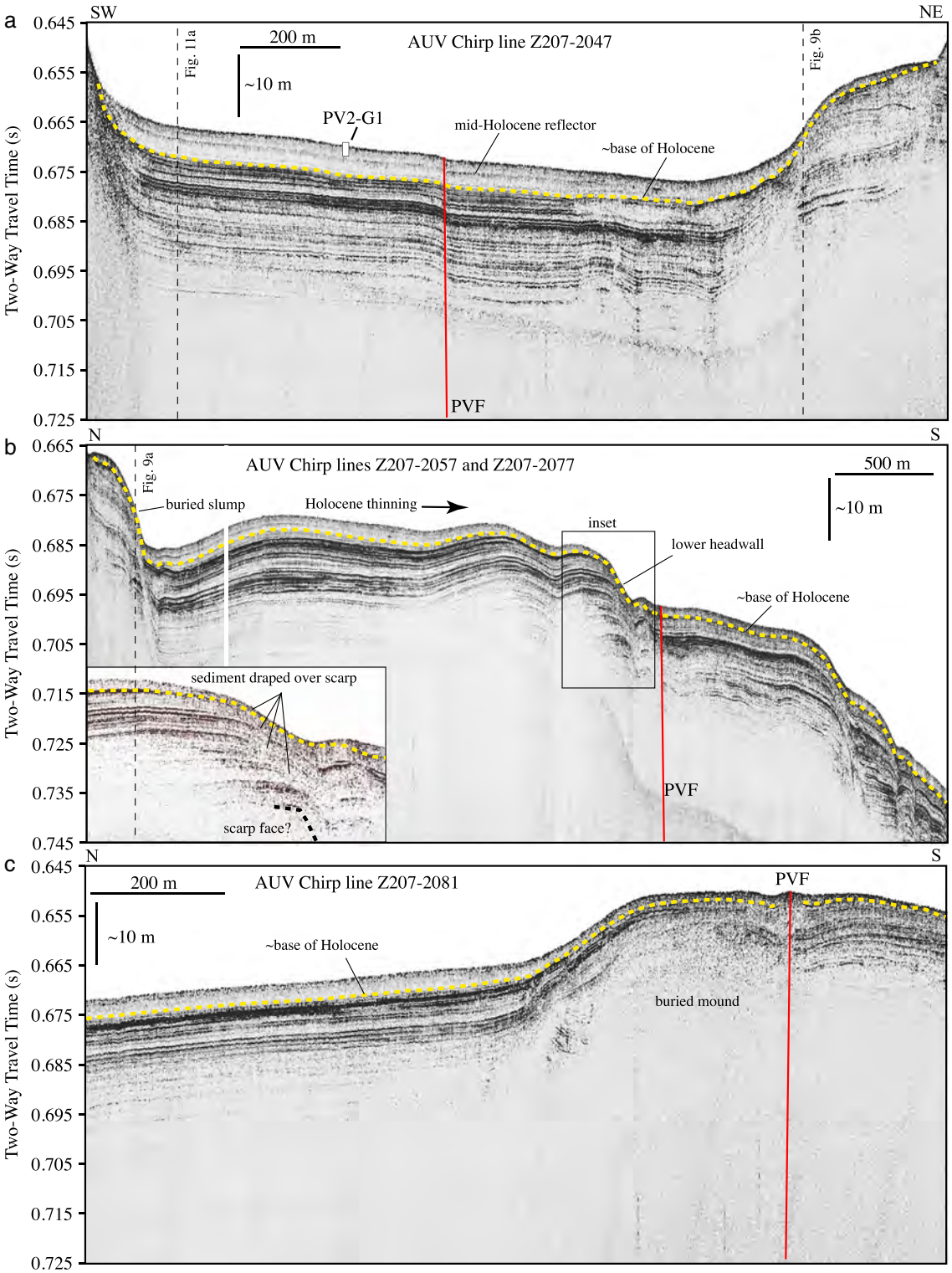

Figure 9. Select AUV chirp profiles below the upper headwall (see Figure 3 for locations). (a) Strike line across core PV2-G1 (see Figure 5). Yellow line marks the base of the Holocene section. (b) Dip line across the upper and lower headwalls. Note the significant thickness of sediment drape on both features. Enlarged inset highlights the drape deposit on the lower headwall. (c) Dip line across the offset mound.

profiles show a faint mid-Holocene reflector, estimated to be emplaced ~5 kyr B.P. (Figures 9a and 9b). Holocene and late Pleistocene strata show thinning and sometimes onlap toward bathymetric highs, particularly above the bathymetric mound and buried slump (Figures 3b and 9). Layers emplaced above the lower headwall show thinning and some downlap toward the top edge of the lower headwall (Figure 9b), suggesting the scarp existed prior to the emplacement of the layers.

5. Interpretations

5.1. Stratigraphic and Depositional Evidence for Headwall Age

An isopach map of Holocene sediment thickness delineates three significant Holocene depocenters within the AUV survey area, and each is associated with an abrupt change in seabed gradient (black arrows in Figure 10). This observation provides important constraints on the dominant mode of sediment delivery to the study area, which in turn is used to understand the interplay between strike-slip fault geometry, seabed morphology, and depositional processes. The shallowest depocenter is located along the fault-bound channel between the 350 m and 400 m isobaths (Figures 3a and 10b). The upslope edge of this depocenter coincides with a change in seabed gradient from ~1.9° to $<$0.5° (Figure 10b) that is also associated with a slight releasing bend along the PVF. A second break in gradient defines the upslope edge of the fault-bounded pull-part basin, where the seabed gradient along the PVF drops from ~1.2° to $<$0.5°. The basin has been filled with a relatively thick section of Holocene sediment and a series of broad sediment waves (Figures 3a, 7, 8a, and 10c). Near the upper headwall rollover, the Holocene sediment thickness decreases substantially (vibracore DR126 VC-93; Figures 5 and 8a). Lastly, the largest Holocene depocenter imaged in the AUV survey is located below the upper headwall scarp. The headwall scarp is exceptionally steep (20–45°), but the seabed below the headwall is actually back sloped at ~0.5°.

The depositional patterns and stratal geometry observed above the upper headwall scarp can be used to constrain the age of the scarp. We propose that Holocene sediment flows sourced from the shelf edge and upper slope were funneled down the slope along the channel that follows the active trace of the PVF. Gentler seabed gradients associated with transtensional fault bends led to enhanced deposition and formation of small depocenters. The thinning and downlap observed along late Pleistocene and Holocene strata above the headwall (Figures 8a and 8c) suggest these layers were emplaced by sediment flows with hydrodynamics influenced by the presence of the adjacent scarp face. We propose that sediment flows accelerated across the top edge of the headwall scarp, which induced depositional bypass and stratigraphic thinning. Layers above the headwall that exhibit marked thickening toward the scarp (Figures 8a and 8c) were likely emplaced prior to the scarp formation. Therefore, the age of the upper headwall scarp can be bracketed by the age of the thinning/downlapping packages. The oldest and best estimate for the age of the scarp is ~31 ka, the age of the basal horizon that separates the contrasting stratal geometries (i.e., green horizon in Figure 8a).

The landslide that produced the upper headwall and associated sidewall scarps evacuated a 40–80 m thick section of sediment over an area at least 7 km^2, an event expected to emplace a distinctive chronostratigraphic marker bed discernable in seismic reflection profiles. A Huntec DTS profile across the landslide evacuation zone shows a ~45 m thick section of well-stratified reflectors above an acoustically chaotic layer of unknown thickness (Figure 11). We interpret the chaotic layer to be the mass transport deposit emplaced by failure of the upper landslide at ~31 ka, providing an estimate of the average sedimentation rate over this interval. The stratified section above the failure horizon likely represents postfailure accumulation of turbidites and hemipelagic drape. Between the upper and lower headwalls, the total thickness of the 31–10 ka section is 38 ± 3 m (Figure 11), yielding an average sedimentation rate of 1.67–1.95 mm/yr, which is significantly higher than the maximum average Holocene rate of 0.55 mm/yr in the same area, but reasonable based on other estimates in the ICB [*Normark et al.*, 2009a].

The buried portion of the lower headwall scarp truncates strata that were emplaced above the 31 ka horizon (Figure 11b), suggesting the lower scarp formed during a landslide sometime after 31 ka. To estimate the age of the lower landslide, we apply digital flattening to the basal Holocene reflector and use stratal thickness and acoustic character to identify positive correlation between layers above and below the lower headwall scarp (Figure 11c). Layers deposited above the blue horizon can be matched on either side of the buried scarp.

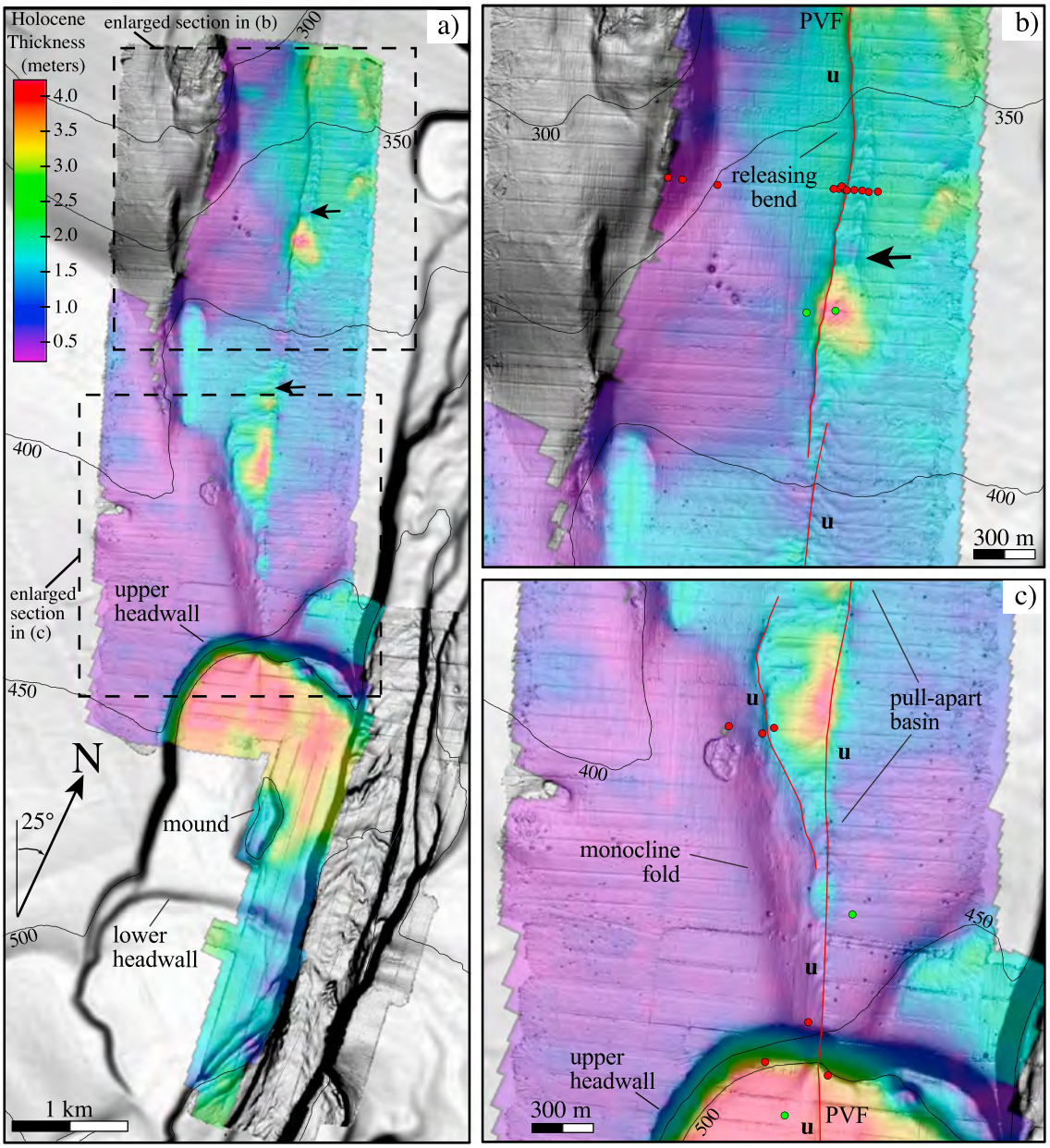

Figure 10. (a) Holocene sediment thickness isopach draped over shaded relief bathymetry. (b) Enlarged area surrounding the first major change in channel gradient and associated depocenter. (c) Enlarged view of the depocenter associated with the pull-apart basin and top edge of the upper headwall scarp. Dots represent core locations (see Figure 3).

Below the blue horizon, strata above the scarp are truncated and show little to no correlation with the acoustically chaotic section below the scarp, implying the original seabed scarp had ~20 m of relief that has been reduced to ~10 m by subsequent deposition at the base of the scarp. The sediment thickness between the blue horizon and the ~31 ka horizon varies from 14 to 24 m. Thus, the average late Pleistocene sedimentation rates estimated above can be used to bracket the age of the lower landslide to 17–24 ka.

The geomorphic development of the Palos Verdes slide scars is summarized in Figure 12.

1. The upper landslide failure occurred ~31 ka, forming an 80 m high scarp. Both the buried slump and bathymetric mound are located within the evacuation zone and appear to be buried masses of cohesive sediment emplaced during the landslide. Both were subsequently buried by >20 m of sediment (Figure 9).

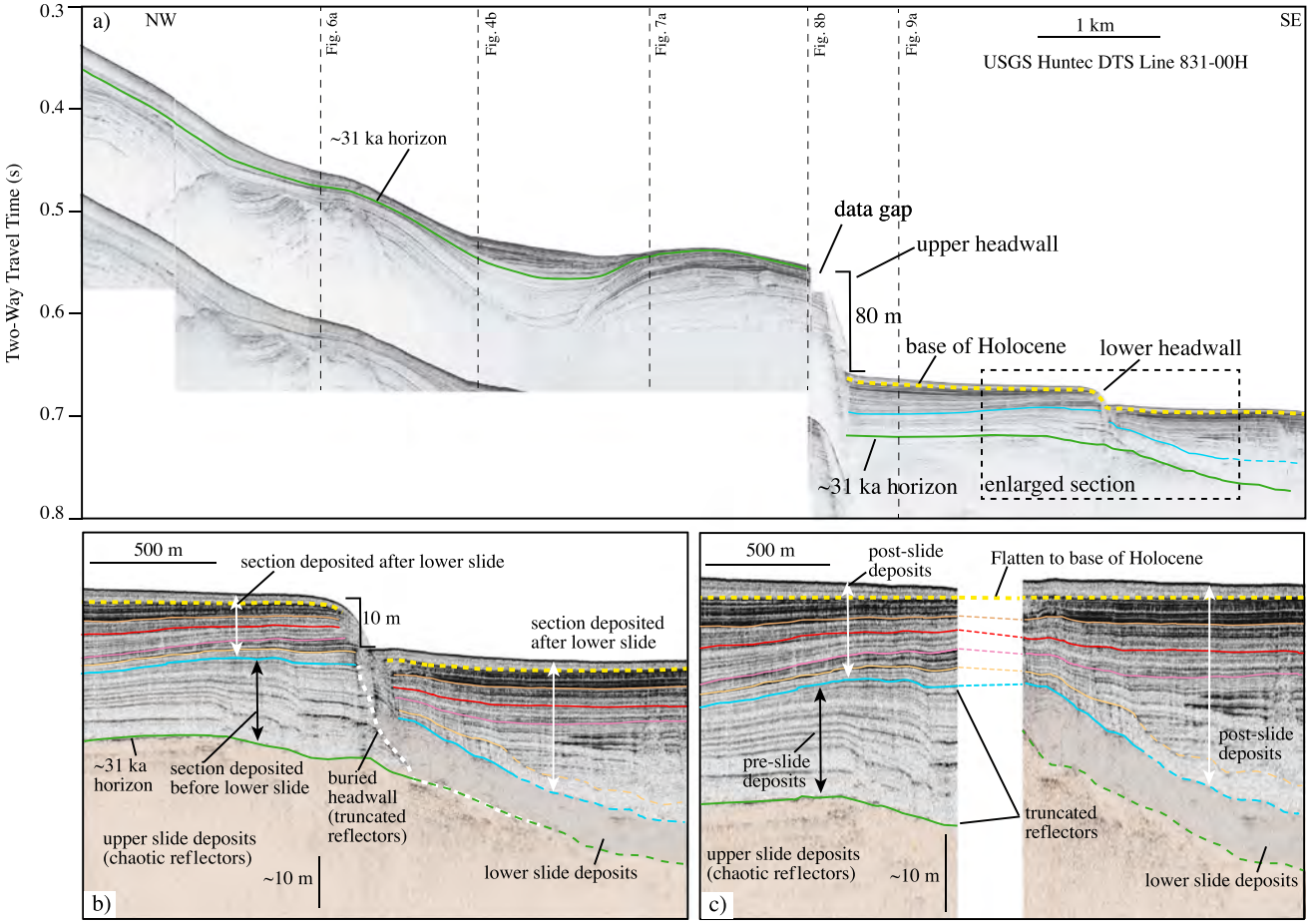

Figure 11. (a) Huntec deep-tow seismic (DTS) reflection profile spanning the AUV survey (see Figure 3 for location and see text for description of horizon interpretations). (b) Enlarged section over lower headwall scarp. Interpretations are based on stratigraphic correlations across the scarp. (c) Same as Figure 11b, but with horizon flattening applied to the approximate base of the Holocene section (yellow).

2. Sediment flows passing over the upper headwall bypassed the steep scarp and deposited material at its base between 31 and 24–17 ka.
3. Sometime between 24 and 17 ka, the lower landslide occurred and formed a 20 m high scarp.
4. Sediment flows passing over the upper headwall continued to bypass the steep scarp face and accumulate on the seafloor below, burying the mound, slump, and the lower headwall (Figures 9 and 11).

5.2. Displacement Analysis, Slip Rate Estimates, and Holocene Activity

Two approaches were used to reconstruct the fault displacement. First, the AUV bathymetry grid was cut along the PVF, yielding two separate bathymetric surfaces that could be geospatially shifted along the trace of the fault. The surface on the eastern side of the fault was incrementally back slipped to realign piercing points. The best fit reconstruction was selected from visual analysis of 3-D perspective views (Figures 13–16). Second, bathymetric profiles orthogonal to offset features were extracted from the AUV bathymetry and projected into a coordinate system whose origin is defined by the trace of the PVF. This allows for comparison of relative offset along either side of the PVF. The primary source of uncertainty is in determining the orientation of offset features and the projected trend of those features onto the PVF. In each case, at least two profiles were used to account for the range of permissible values (Figures 14–16). Back slip was applied to profiles along the eastern side of the PVF until the correlative morphology aligned; the mismatch among profiles provided an uncertainty envelope.

Southwest facing perspective views from the top of the upper headwall show the intersection of the PVF with the scarp (Figure 14a). The scarp face is asymmetric across the fault. However, a small facet along

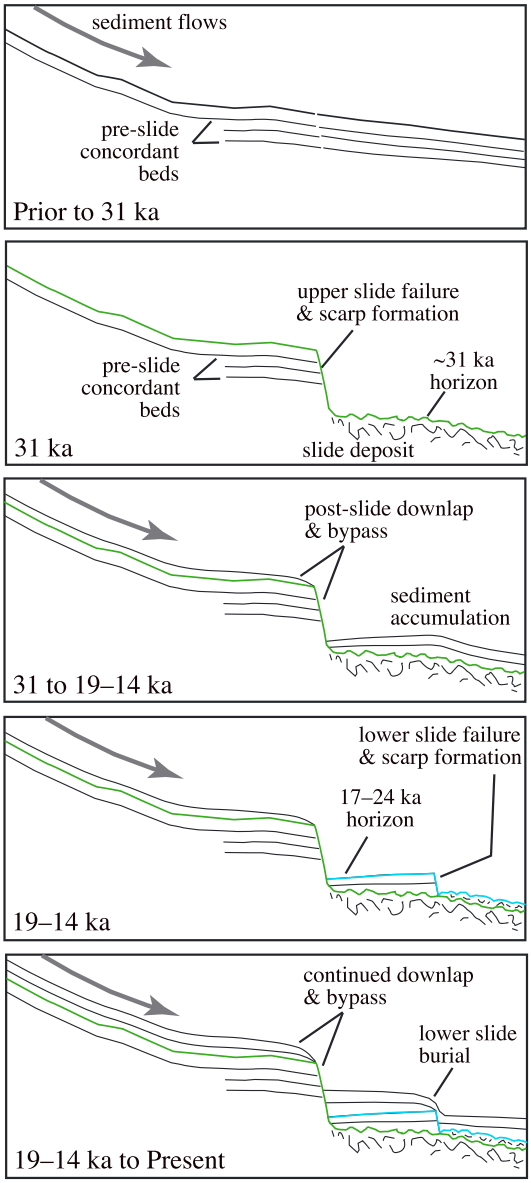

Figure 12. Interpretive schematic cartoon summarizing the geomorphic development of features observed in Figure 11. Initial deposition resulted in relatively flat and continuous reflections (prior to 31 ka). At ~31 ka, a failure event truncated reflections at the upper headwall. Subsequent sediment flows deposited packages that downlap onto and bypass the upper headwall, leading to accumulation of relatively flat reflections at the base of the upper headwall (31 to 24–17 ka). A later failure (24–17 ka) truncated reflections at the base of the upper headwall and created the lower headwall. Sediment flows continued to bypass the upper headwall, and hemipelagic deposition likely contributed to deposition draping the lower headwall (24–17 ka to Present).

the eastern scarp is interpreted to be the original scarp face that has been offset by the PVF (marked "east face" in Figures 14a–14c). After 55 m of back slip (Figure 14d), an alignment is apparent in the shape and trend of the eastern and western scarp faces, as well as in the alignment of bathymetric contours (Figures 14d–14f). The margin of error in the reconstruction is estimated to be ±5 m (half width of the uncertainty envelope). The same procedure was applied to the offset mound (Figure 15) and the lower headwall (Figure 16). A south facing perspective view shows misalignment of the eastern face of the mound. A 40 m wide surface mask was applied to the southwestern edge of the PVF to remove localized folding and deformation. The piercing points are defined by the upper edge of the mound, coincident with the trend of maximum curvature. The total displacement is estimated to be 52 ± 4 m. The morphology and trend of the lower headwall scarp varies on either side of the PVF (Figure 16). Bathymetric contours that warp into the fault trace suggest distributed deformation across ~100 m wide fault zone may be responsible for the morphological differences. Therefore, we identify the original scarp face on either side the PVF by examining sections of the sloped seafloor away from the fault that contain parallel contours and roughly the same seafloor gradient. We assume that strike lines drawn across the offset faces and extended toward the PVF would have intersected at the PVF when the scarp originally formed prior to displacement (Figure 16a). The strike lines intersect and scarp profiles align following 39 ± 8 m of back slip.

Age (31 ka) and displacement (55 ± 5 m; 52 ± 4 m) estimates for the upper headwall and mound yield right-lateral slip rates of 1.6–1.9 mm/yr and 1.5–1.9 mm/yr, respectively. The age (17–24 ka) and displacement (39 ± 8 m) estimates for the lower headwall yield an average right-lateral slip rate of 1.3–2.8 mm/yr. The estimates derived from three independent piercing points show agreement; hence, our best estimate for the slip rate of the PVF since 31 ka is 1.6–1.9 mm/yr. Because the fault appears to merge into a single active strand within the AUV survey area and takes on a near-vertical dip in the upper 2 km (e.g., Figure 4), we propose that these slip rates reflect most, if not all, of the right-lateral slip budget of the PVF between the shelf edge and Lasuen Knoll.

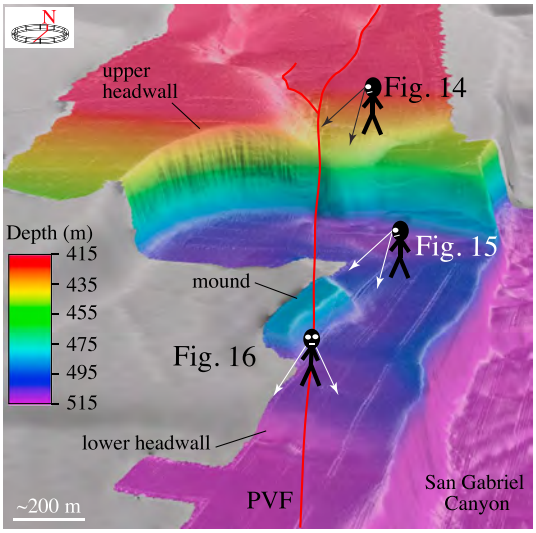

Figure 13. Points of reference for perspective views for each of the three piercing points used in the offset reconstruction: upper headwall (Figure 14), buried mound (Figure 15), and lower headwall (Figure 16).

Offset reflectors and seafloor lineaments provide clear evidence that the PVF experienced Holocene ruptures. However, constraining the age of Holocene events, the average displacement per event, and the total number of events over a given time interval is difficult due to the absence of Holocene age piercing points. The record of vertical faulting in the pull-apart basin offers the best evidence for growth faulting, which can be used to identify Holocene ruptures [e.g., *Brothers et al.*, 2011]. The seafloor, horizon HB (dashed red line in Figure 7c), and the basal Holocene reflector in the pull-apart basin each steepen into the PVF and show increasing dip down section. Offset reflections, deformation, and changes in thickness of the sedimentary packages bounded by these three horizons suggest there have been at least three Holocene ruptures, each producing ~0.5 m of vertical growth (Figure 7b). The first appears to have occurred during the early Holocene, offsetting the basal horizon, the second occurred in the middle Holocene and offsetting horizon HB, and the third likely occurred in the recent past (i.e., last few hundred years) based on clear evidence for seafloor offset (Figure 7c). However, this approach is limited by our ability to resolve evidence for vertical growth in the subbottom profiles, and we cannot rule out additional events that did not produce vertical subsidence or were not recorded as punctuated growth faulting in the stratigraphic record.

Evidence of sediment gravity flow deposits in the pull-apart basin suggests that the three displacement events inferred from the chirp subbottom profile are a minimum estimate of Holocene activity. Although bioturbation has partially obscured bed continuity and contacts, there is evidence in core DR136 VC-134 for up to 18 event beds (Figure 7b and Data Set S1). These turbidites are primarily very fine to fine-grained sand and mud, and many contain concentrated terrestrial woody organic material that was transported into the slope depositional environment. Because the gullies and San Gabriel Canyon head are many kilometers from the shoreline and were likely disconnected from longshore drift cells and fluvial sediment input by sea level rise during the Holocene [*Lambeck and Chappell*, 2001; *Normark et al.*, 2009b], turbidites in DR136 VC-134 were likely generated from submarine landslides along the shelf edge and upper slope that may have been triggered by earthquakes along the PVF. However, given the abundance of active faults proximal to the study area (within 100 km), only speculative linkages between individual event beds in DR136 VC-134 and paleo-earthquakes on the PVF can be made.

The approach developed by *Wells and Coppersmith* [1994] and previously applied to the PVF by *Stephenson et al.* [1995] is used to calculate the potential magnitude of Holocene earthquakes along the PVF. Although the PVF geometry is poorly constrained at depth, the 42–50 km stretch between the inner San Pedro Shelf and Lasuen Knoll does not appear to have major structural boundaries precluding a thoroughgoing rupture [*Fisher et al.*, 2004b]. Using the 1.6–1.9 mm/yr average slip rate since ~31 ka, we can assume the fault accommodated between 16 and 19 m of offset during the Holocene. Given the stratigraphic evidence for at least three Holocene ground ruptures, each producing an inferred 5–7 m of right-lateral offset, a through-going rupture of the PVF from the inner San Pedro Shelf to Lasuen Knoll has the potential to generate a *M*7.3 earthquake.

6. Discussion

The basic starting point in understanding the earthquake threat that the PVF poses to metropolitan areas in Southern California is to identify the predominant mode of coseismic displacement. For years, researchers

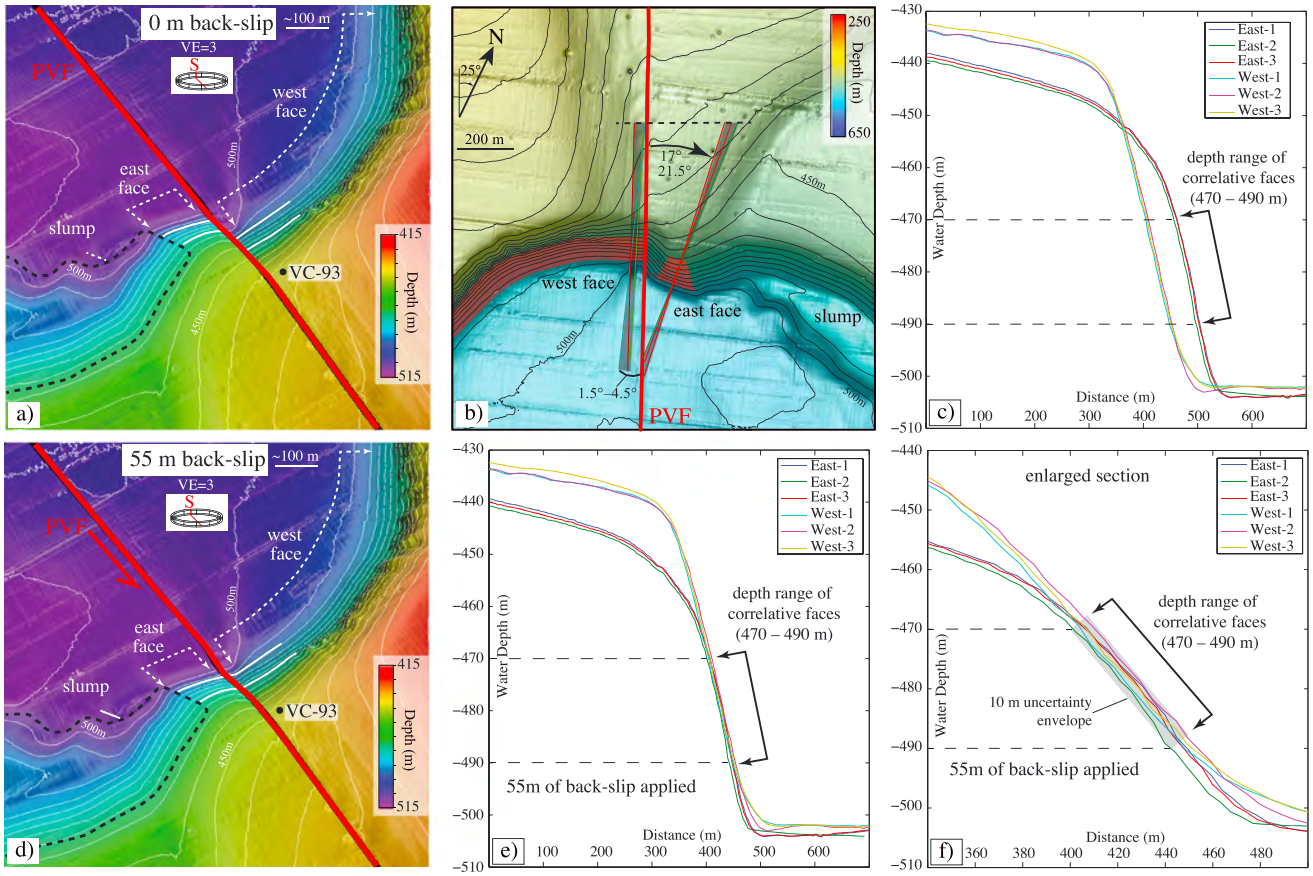

Figure 14. Offset reconstruction for the upper headwall scarp. (a) Perspective view of the present-day configuration from above the upper headwall scarp looking to the southwest and oblique to the Palos Verdes Fault (PVF; see Figure 13 for point of reference). Present-day configuration (0 m back slip). (b) Map view of offset scarp faces and locations of bathymetric profiles used to reconstruct offset (see text for details). Dashed line represents the baseline for a common coordinate system; angles are used to project profiles onto the trace of the PVF. (c) Bathymetric profiles after projection onto the PVF. (d) Perspective view following 55 m of back slip applied to the eastern digital elevation model (DEM) surface. (e) Profile plot following 55 m of back slip applied to profiles crossing the eastern scarp face. (f) Enlarged view of Figure 14e showing correlative faces and uncertainty envelope (10 m).

have argued that the PVF accommodates limited strike-slip motion and instead is primarily a thrust or reverse-oblique fault system [*Brankman and Shaw*, 2009; *Shaw and Suppe*, 1996; *Sorlien et al.*, 2013], while others argued in favor of strike-slip dominance where transpression and transtension result from restraining and releasing bends [*Bohannon and Geist*, 1998; *Fisher et al.*, 2004b; *McNeilan et al.*, 1996; *Legg et al.*, 2007; *Ryan et al.*, 2012, 2009]. Despite limited constraints on fault geometry at depth, thrust/reverse faulting cannot account for the ~55 m of late Pleistocene and Holocene horizontal displacement documented in this study, nor can a thrust model account for the strong link between subtle bends and jogs in the trend of the PVF and transtensional/transpressional deformation (e.g., the pull-apart basin observed in the AUV data). The observed displacement and geomorphic expression of the PVF provide a compelling argument that the PVF is a near-vertical strike-slip fault down to the base of the seismogenic zone as argued by *Fisher et al.* [2004b]. As new high-resolution marine geophysical data become available, strike-slip dominance of faults in the ICB is becoming more apparent [*Legg et al.*, 2007; *Ryan et al.*, 2012, 2009].

Slip rate estimates constrained by high-resolution data and direct observations in this study should trigger reconsideration of existing slip rate estimates along the PVF. Our best estimate for the right-lateral slip rate is roughly half of previous estimates [e.g., *McNeilan et al.*, 1996; *Stephenson et al.*, 1995]; offset interpretations and uncertainties in slip rate estimates along the Palos Verdes Shelf may need to be revisited using modern geophysical imaging techniques. Although the higher-resolution geophysical data and targeted sampling in this study allowed for identification of active structures, precise measurement and reconstruction of offset, and targeted dating, this study also benefited from the relatively simple geometry and near-bottom

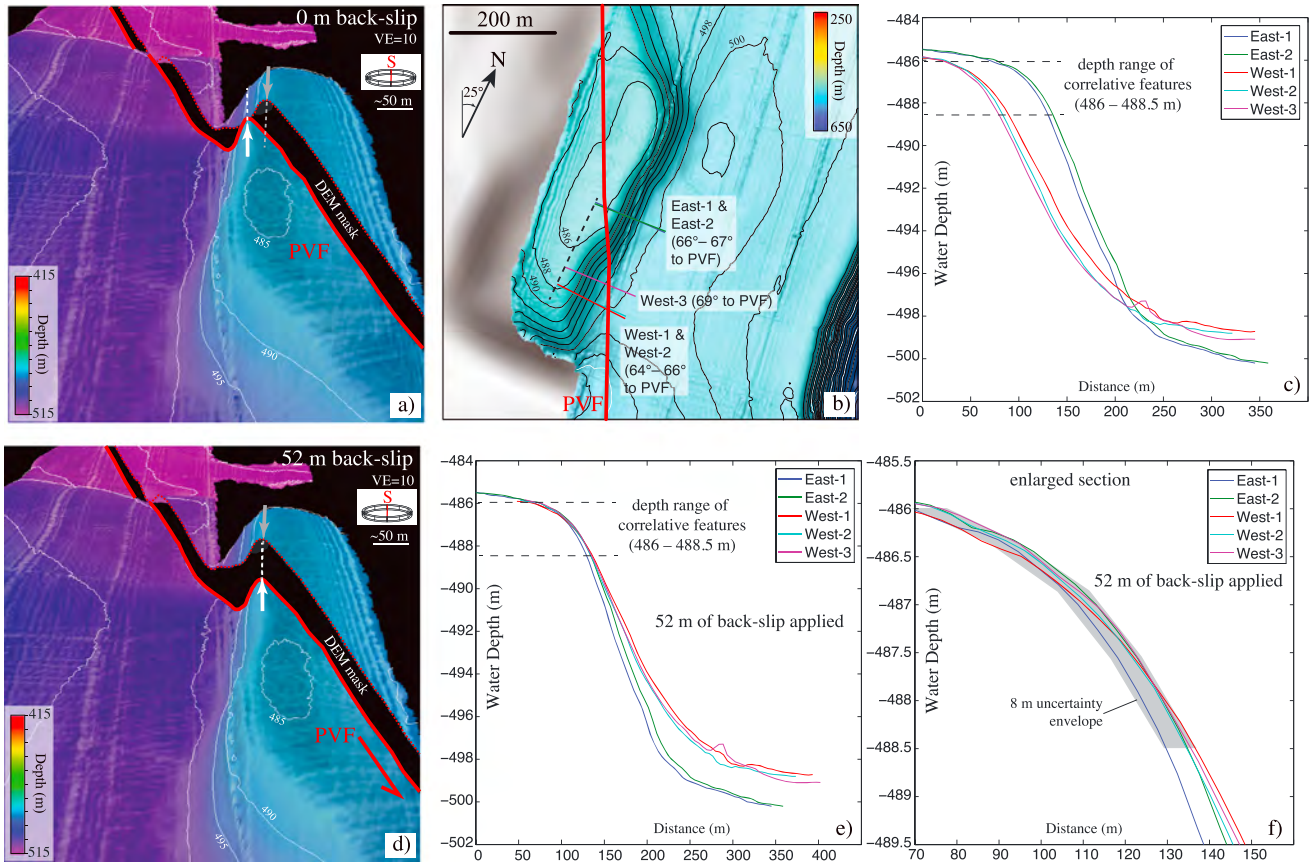

Figure 15. Offset reconstruction for the seafloor mound. (a) Perspective view of the present-day configuration from above the mound looking to the southwest and oblique to the Palos Verdes Fault (PVF; see Figure 13 for point of reference). Piercing point is the upper edge of the mound. (b) Map view of offset mound and locations of bathymetric profiles used to reconstruct offset (see text for details). Dashed line represents the baseline for a common coordinate system; angles are used to project profiles onto the trace of the PVF. Correlative features are the zone of maximum curvature along the upper edge of the mound. (c) Bathymetric profiles after projection onto the PVF. (d) Perspective view following 52 m of back slip applied to the eastern DEM surface. (e) Profile plot following 52 m of back slip applied to profiles crossing the eastern scarp face. (f) Enlarged view of Figure 15e showing correlative edges and uncertainty envelope (8 m).

expression of the PVF in the study area. The close correlation between changes in fault orientation and sense of vertical offset observed in the AUV data (Figure 3) suggests that uplift and subsidence along the PVF are the result of transpressional and transtensional bends that are characteristic of nearly all strike-slip faults [*Christie-Blick and Biddle*, 1985; *Sylvester*, 1988].

There is, at present, no clear consensus on how slip is partitioned and how it transfers between individual faults throughout the ICB, owing in large part to uncertainty in mapping of active fault traces and to the lack of reliable slip rate estimates on the various fault strands. The PVF slip rate estimate in this study (1.6–1.9 mm/yr) represents ~20–32% of the ~6–8 mm/yr of the relative plate motion accommodated by the ICB [*Bennett et al.*, 1996; *Platt and Becker*, 2010]. Within the ICB, only the PVF (this study) and the San Diego Trough Fault (1.2–1.8 mm/yr [*Ryan et al.*, 2012]) have slip rate estimates for sections in water depths greater than 200 m. Combined, these faults may take on 40–70% of the slip budget for the ICB. However, the PVF appears to die out to the south of Lasuen Knoll [*Brankman and Shaw*, 2009; *Ryan et al.*, 2009]; how deformation is transferred from the PVF to other faults is unresolved. The Newport-Inglewood Fault may carry between 1 and 2 mm/yr of dextral slip to the south of Dana Point [*Fischer and Mills*, 1991] and carries a minimum of 0.34–0.55 mm/yr farther north near Huntington Beach [*Grant et al.*, 1997]. It is not clear how the Newport Inglewood Fault interacts with east dipping faults on the continental slope offshore Dana Point [*Ryan et al.*, 2009] or with possible thrust faults that are inferred to underlie much of the ICB [*Rivero et al.*, 2000]. One possibility is that dextral slip is transferred offshore from the Newport-Inglewood Fault, across a discontinuous system of faults along the northeastern side of Lasuen Knoll,

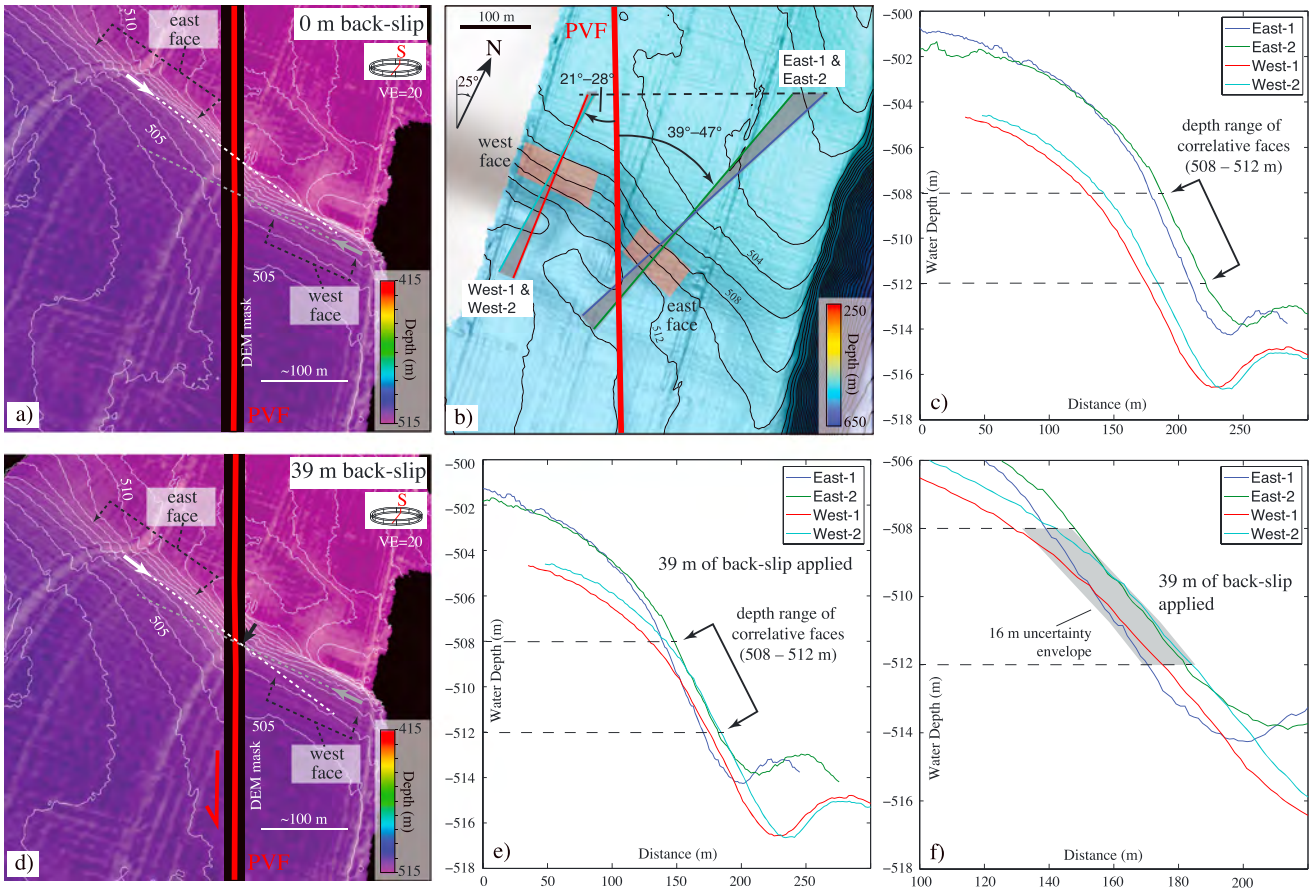

Figure 16. Offset reconstruction for the lower headwall. (a) Perspective view of the present-day configuration from above the lower headwall and oblique to the Palos Verdes Fault (PVF; see Figure 13 for point of reference). Dashed lines and arrows mark the trend of the original scarp faces prior to offset. (b) Map view of offset faces and locations of bathymetric profiles used to reconstruct offset (see text for details). Dashed line represents the baseline for a common coordinate system; angles are used to project profiles onto the trace of the PVF. (c) Bathymetric profiles after projection onto the PVF. (d) Perspective view following 39 m of back slip applied to the eastern DEM surface. (e) Profile plot following 39 m of back slip applied to profiles crossing the eastern scarp face. (f) Enlarged view of Figure 16e showing correlative faces and uncertainty envelope (16 m).

and onto the PVF. If correct, the majority of the remaining ICB slip budget at the latitude of the study area (3–5 mm/yr) may be accommodated by the San Clemente Fault.

7. Conclusions

The high-resolution AUV and ROV data in this study provide the best available constraints on fault location, mode of coseismic deformation, and late Pleistocene and Holocene slip rate for the offshore extension of the PVF. Along-strike bends in the orientation of the PVF are associated with transpressional ridges (restraining bends) and pull-apart basins (releasing bends), which influence both the geomorphic development of the continental slope and also the spatial distribution of sediment dispersal pathways and Holocene depocenters. Three separate geomorphic features along the lower slope show primary evidence for right-lateral offset by the PVF, providing a set of piercing points that were used to generate a best estimate for the late Pleistocene and Holocene slip rate (1.6–1.9 mm/yr). Vertical growth faulting observed in a small pull-apart basin suggests at least three ruptures occurred during the Holocene with a potential magnitude of greater than M_w 7. The fault morphology, right-lateral displacement and horizontal slip rate estimates provide convincing evidence that the PVF is a steeply dipping strike-slip fault [e.g., *Fisher et al.*, 2004b] and is unlikely to have direct kinematic linkages to proposed low-angle thrust/reverse faults at depth [e.g., *Shaw and Suppe*, 1996; *Brankman and Shaw*, 2009]. Results from this study can be incorporated into future earthquake and hazard assessment models and may require updates to existing maps and models [e.g., *USGS and California Geological Survey*, 2014; *Field et al.*, 2013, 2014; *Parsons et al.*, 2013].

Acknowledgments
Funding was provided by the Monterey Bay Aquarium Research Institute through the David and Lucile Packard Foundation and by the USGS Coastal and Marine Geology Program. Special thanks are given to the MBARI autonomous underwater vehicle (AUV) Operations Group, the MBARI remotely operated vehicle (ROV) pilots, and the crews and science parties of the R/V *Zephyr*, R/V *Western Flyer*, and R/V *Sproul*. We also thank Krystle Anderson, Eve Lundsten, Holly Ryan, Brian Edwards, Mike Torresan, Peter Dartnell, Ray Sliter, and Florence Wong for data assistance and discussions. Tom Parsons and Nathan Miller provided helpful reviews. Seismic reflection data in this study are archived at the USGS Pacific Coastal and Marine Science Center. Data not posted to public servers (e.g., https://walrus.wr.usgs.gov/NAMSS/ and https://walrus.wr.usgs.gov/infobank/) are available from the corresponding author upon request. Mention of trade names does not imply U.S. Government endorsement of commercial products.

References

Astiz, L., and P. M. Shearer (2000), Earthquake locations in the inner Continental Borderland, offshore Southern California, *Bull. Seismol. Soc. Am.*, *90*(2), 425–449.

Atwater, B. F., B. Carson, G. B. Griggs, H. P. Johnson, and M. S. Salmi (2014), Rethinking turbidite paleoseismology along the Cascadia subduction zone, *Geology*, *42*(9), 827–830.

Atwater, T., and J. Stock (1998), Pacific-North America plate tectonics of the Neogene southwestern United States: An update, *Int. Geol. Rev.*, *40*(5), 375–402.

Barnes, P. M., and N. Pondard (2010), Derivation of direct on-fault submarine paleoearthquake records from high-resolution seismic reflection profiles: Wairau Fault, New Zealand, *Geochem. Geophys. Geosyst.*, *11*, Q11013, doi:10.1029/2010GC003254.

Bartholomew, T. D., T. A. Little, K. J. Clark, R. Van Dissen, and P. M. Barnes (2014), Kinematics and paleoseismology of the Vernon Fault, Marlborough Fault System, New Zealand: Implications for contractional fault bend deformation, earthquake triggering, and the record of Hikurangi subduction earthquakes, *Tectonics*, *33*, 1201–1218, doi:10.1002/2014TC003543.

Bennett, R. A., W. Rodi, and R. E. Reilinger (1996), Global Positioning System constraints on fault slip rates in Southern California and northern Baja, Mexico, *J. Geophys. Res.*, *101*(B10), 21,943–21,960, doi:10.1029/96JB02488.

Bohannon, R. G., and E. Geist (1998), Upper crustal structure and Neogene tectonic development of the California continental borderland, *Geol. Soc. Am. Bull.*, *110*(6), 779–800.

Brankman, C. M., and J. H. Shaw (2009), Structural geometry and slip of the Palos Verdes fault, Southern California: Implications for earthquake hazards, *Bull. Seismol. Soc. Am.*, *99*(3), 1730–1745.

Brothers, D. S., G. M. Kent, N. W. Driscoll, S. B. Smith, J. A. Dingler, A. J. Harding, G. G. Seitz, R. Karlin, and J. M. Babcock (2009), New constraints on earthquake history and slip-rates on the West Tahoe-Dollar Point Fault, Lake Tahoe Basin, CA, *Bull. Seismol. Soc. Am.*, *99*(2A), 499–519.

Brothers, D. S., D. Kilb, K. Luttrell, N. W. Driscoll, and G. M. Kent (2011), Loading of the San Andreas fault by flood-induced rupture of faults beneath the Salton Sea, *Nat. Geosci.*, *4*(7), 486–492, doi:10.1038/ngeo1184.

Caess, D. W., H. Thomas, W. J. Kirkwood, R. McEwen, R. Henthorn, D. A. Clague, C. K. Paull, J. Paduan, and K. L. Maier (2008), *High-Resolution Multibeam, Sidescan, and Subbottom Surveys Using the MBARI AUV D. Allan B*, Alaska Sea Grant College Program, Univ. of Alaska, Fairbanks.

Christie-Blick, N., and K. T. Biddle (1985), Deformation and basin formation along strike-slip faults, *Strike-Slip Deformation, Basin Formation, and Sedimentation*, SEPM Spec. Pap., (SP37).

Crouch, J. K., and J. Suppe (1993), Late Cenozoic tectonic evolution of the Los Angeles basin and inner California borderland: A model for core complex-like crustal extension, *Geol. Soc. Am. Bull.*, *105*(11), 1415–1434.

Dartnell, P., and J. V. Gardner (2009), Seafloor terrain analysis and geomorphology of the greater Los Angeles margin and San Pedro basin, Southern California, in *Earth Science in the Urban Ocean: The Southern California Continental Borderland*, edited by H. Lee and W. Normark, *Geol. Soc. Am. Spec. Pap.*, *454*, 9–28.

Dartnell, P., J. E. Conrad, H. F. Ryan, and D. P. Finlayson (2014), Bathymetry and Acoustic Backscatter—Outer Mainland Shelf and Slope, Gulf of Santa Catalina, Southern California, *U.S. Geol. Surv. Open File Rep.*, *1094*, 15, doi:10.3133/ofr20141094.

Dartnell, P., N. W. Driscoll, D. S. Brothers, J. E. Conrad, J. A. Kluesner, and G. M. Kent (2015), Colored shaded-relief bathymetry, acoustic backscatter, and selected perspective views of the Inner Continental Borderland, Southern California, *U.S. Geol. Surv. Sci. Invest. Map*, *3324*, 3, doi:10.3133/sim3324.

DeMets, C., R. G. Gordon, and D. F. Argus (2010), Geologically current plate motions, *Geophys. J. Int.*, *181*(1), 1–80.

Dingler, J. A., G. Kent, N. Driscoll, J. M. Babcock, A. J. Harding, G. G. Seitz, R. Karlin, and C. Goldman (2009), A high-resolution seismic CHIRP investigation of active normal faulting across the Lake Tahoe Basin, California-Nevada, *Geol. Soc. Am. Bull.*, *121*(7/8), 1089–1107.

Field, E. H., et al. (2013), Uniform California earthquake rupture forecast, version 3 (UCERF3)—The time-independent model, *U.S. Geol. Surv. Open File Rep.*, *1165*, 97.

Field, E. H., R. J. Arrowsmith, G. P. Biasi, P. Bird, T. E. Dawson, K. R. Felzer, D. D. Jackson, K. M. Johnson, T. H. Jordan, and C. Madden (2014), Uniform California Earthquake Rupture Forecast, Version 3 (UCERF3)—The time-independent model, *Bull. Seismol. Soc. Am.*, *104*(3), 1122–1180.

Fischer, P. J., and G. I. Mills (1991), The offshore Newport–Inglewood– Rose Canyon fault zone, California: Structure, segmentation and tectonics, in *Environmental Perils San Diego Region*, *Geol. Soc. Am. Annu. Meet.*, edited by P. L. Abbott and W. J. Elliot, pp. 17–36, San Diego Assoc. of Geologists, San Diego, Calif.

Fischer, P. J., R. H. Patterson, C. Darrow, J. H. Rudat, and G. Simila (1987), The Palos Verdes fault zone: Onshore to offshore, in *Geology of the Palos Verdes Peninsula and San Pedro Bay, Pacific Section SEPM and AAPG Field Trip Guide Book*, vol. 55, edited by P. J. Fischer, pp. 91–133, SEPM, Tulsa, Okla.

Fisher, M. A., W. R. Normark, V. E. Langenheim, A. J. Calvert, and R. W. Sliter (2004a), Marine geology and earthquake hazards of the San Pedro shelf region, Southern California, *U.S. Geol. Surv. Prof. Pap.*, *1687*, 39.

Fisher, M. A., W. R. Normark, V. E. Langenheim, A. J. Calvert, and R. W. Sliter (2004b), The offshore Palos Verdes Fault Zone near San Pedro, Southern California, *Bull. Seismol. Soc. Am.*, *94*(2), 506–530.

Gardner, J. V., and P. Dartnell (2002), Multibeam mapping of the Los Angeles, California margin, *U.S. Geol. Surv. Open File Rep.*, *OF02-162*.

Goldfinger, C. (2011), Submarine paleoseismology based on turbidite records, *Annu. Rev. Mar. Sci.*, *3*, 35–66.

Grant, L. B., and P. M. Shearer (2004), Activity of the offshore Newport-Inglewood Rose Canyon fault zone, coastal Southern California, from relocated microseismicity, *Bull. Seismol. Soc. Am.*, *94*(2), 747–752.

Grant, L. B., J. T. Waggoner, T. K. Rockwell, and C. von Stein (1997), Paleoseismicity of the north branch of the Newport-Inglewood fault zone in Huntington Beach, California, from cone penetrometer test data, *Bull. Seismol. Soc. Am.*, *87*(2), 277–293.

Ingram, B. L., and J. R. Southon (1996), Reservoir ages in eastern Pacific coastal and estuarine waters, *Radiocarbon*, *38*(3), 573–582.

Johnson, S. Y., S. R. Hartwell, and P. Dartnell (2014), Offset of Latest Pleistocene shoreface reveals slip rate on the Hosgri strike-slip fault, offshore Central California, *Bull. Seismol. Soc. Am.*, *104*(4), 1650–1662.

Judd, A. G., and M. Hovland (2007), *Seabed Fluid Flow: The Impact of Geology, Biology and the Marine Environment*, vol. XV, 475 pp., Cambridge Univ. Press, Cambridge, New York.

Kent, G. M., et al. (2005), 60 k.y. record of extension across the western boundary of the Basin and Range province: Estimate of slip rates from offset shoreline terraces and a catastrophic slide beneath Lake Tahoe, *Geology*, *33*(5), 365–368.

Lambeck, K., and J. Chappell (2001), Sea level change through the last glacial cycle, *Science*, *292*(5517), 679–686.

Lee, H. J., J. P. M. Syvitski, G. Parker, D. Orange, J. Locat, E. W. H. Hutton, and J. Imran (2002), Distinguishing sediment waves from slope failure deposits: Field examples, including the 'Humboldt slide', and modeling results, *Mar. Geol.*, *192*(1), 79–104.

Legg, M. R. (1991), Developments in understanding the tectonic evolution of the California continental borderland, in *From Shoreline to Abyss*, vol. 46, edited by R. H. Osborne, pp. 291–312, SEPM Shepard Commemorative.

Legg, M. R., C. Goldfinger, M. J. Kamerling, J. D. Chaytor, and D. E. Einstein (2007), Morphology, structure and evolution of California Continental Borderland restraining bends, *Geol. Soc. London Spec. Publ.*, *290*(1), 143–168.
Legg, M. R., M. D. Kohler, N. Shintaku, and D. S. Weeraratne (2015), High-resolution mapping of two large-scale transpressional fault zones in the California Continental Borderland: Santa Cruz-Catalina Ridge and Ferrelo faults, *J. Geophys. Res. Earth Surf.*, *120*, doi:10.1002/2014JF003322.
Lindvall, S. C., and T. K. Rockwell (1995), Holocene activity of the Rose Canyon fault zone in San Diego, California, *J. Geophys. Res.*, *100*(B12), 24,121–24,132, doi:10.1029/95JB02627.
Mann, P. (2007), Global catalogue, classification and tectonic origins of restraining- and releasing bends on active and ancient strike-slip fault systems, *Geol. Soc. London Spec. Publ.*, *290*(1), 13–142, doi:10.1144/sp290.2.
Mann, P., M. R. Hempton, D. C. Bradley, and K. Burke (1983), Development of pull-apart basins, *J. Geol.*, *91*(5), 529–554.
Marlow, M. S., J. V. Gardner, and W. R. Normark (2000), Using high-resolution multibeam bathymetry to identify seafloor surface rupture along the Palos Verdes fault complex in offshore Southern California, *Geology*, *28*(7), 587–590.
McNeilan, T. W., T. K. Rockwell, and G. S. Resnick (1996), Style and rate of Holocene slip, Palos Verdes fault, Southern California, *J. Geophys. Res.*, *101*(B4), 8317–8334, doi:10.1029/95JB02251.
Mix, A. C., D. C. Lund, N. G. Pisias, P. Bodén, L. Bornmalm, M. Lyle, and J. Pike (1999), Rapid climate oscillations in the northeast Pacific during the last deglaciation reflect Northern and Southern Hemisphere sources, *Geophys. Monogr. AGU*, *112*, 127–148.
Nicholson, C., C. C. Sorlien, T. Atwater, J. C. Crowell, and B. P. Luyendyk (1994), Microplate capture, rotation of the western Transverse Ranges, and initiation of the San Andreas transform as a low-angle fault system, *Geology*, *22*(6), 491–495.
NOAA (2014), National Geophysical Data Center, U.S. Coastal Relief Model—Southern California, edited.
Normark, W. R., R. G. Bohannon, R. W. Sliter, G. Dunhill, D. W. Scholl, J. Laursen, J. A. Reid, and S. Olton (1999a), Cruise report for A1-98-SC Southern California Earthquake Hazards Project, *U.S. Geol. Surv. Open File Rep.*, *99-125*, 60.
Normark, W. R., J. A. Reid, R. W. Sliter, D. Holton, C. E. Gutmacher, M. A. Fischer, and J. R. Childs (1999b), Cruise report for 01-99-SC: Southern California Earthquake Hazards Project, *U.S. Geol. Surv. Open File Rep.*, *99-560*, 60.
Normark, W. R., S. Baher, and R. W. Sliter (2004), Late Quaternary sedimentation and deformation in Santa Monica and Catalina basins, offshore Southern California, in *Geology and Tectonics of Santa Catalina Island and the California Continental Borderland, Field Trip Guidebook 32*, pp. 291–317.
Normark, W. R., M. McGann, and R. W. Sliter (2009a), Late quaternary sediment-accumulation rates within the inner basins of the California continental borderland in support of geologic hazard evaluation, in *Earth Science in the Urban Ocean: The Southern California Continental Borderland*, edited by H. Lee and W. Normark, *Geol. Soc. Am. Spec. Pap.*, *454*, 117–140.
Normark, W. R., D. J. Piper, B. W. Romans, J. A. Covault, P. Dartnell, and R. W. Sliter (2009b), Submarine canyon and fan systems of the California Continental Borderland, *Geol. Soc. Am. Spec. Pap.*, *454*, 141–168.
Parsons, T., et al. (2013), Appendix C—Deformation models for UCERF3, *U.S. Geol. Surv. Open File Rep.*, *1165*, 66.
Platt, J. P., and T. W. Becker (2010), Where is the real transform boundary in California?, *Geochem. Geophys. Geosyst.*, *11*, Q06012, doi:10.1029/2010GC003060.
Pondard, N., and P. M. Barnes (2010), Structure and paleoearthquake records of active submarine faults, Cook Strait, New Zealand: Implications for fault interactions, stress loading, and seismic hazard, *J. Geophys. Res.*, *115*, B12320, doi:10.1029/2010JB007781.
Ponti, D. J. (1989), *Aminostratigraphy and Chronostratigraphy of the Pleistocene Marine Sediments, Southwestern Los Angeles Basin, California*, Univ. of Colo., Boulder.
Rivero, C., J. H. Shaw, and K. Mueller (2000), Oceanside and Thirtymile Bank blind thrusts: Implications for earthquake hazards in coastal Southern California, *Geology*, *28*(10), 891–894.
Ryan, H. F., M. R. Legg, J. E. Conrad, and R. W. Sliter (2009), Recent faulting in the Gulf of Santa Catalina: San Diego to Dana Point, in *Earth Science in the Urban Ocean: The Southern California Continental Borderland*, edited by H. Lee and W. Normark, *Geol. Soc. Am. Spec. Pap.*, *454*, 291–315.
Ryan, H. F., J. E. Conrad, C. K. Paull, and M. McGann (2012), Slip rate on the San Diego Trough fault zone, Inner California Borderland, and the 1986 Oceanside earthquake swarm revisited, *Bull. Seismol. Soc. Am.*, *102*(6), 2300–2312.
Shaw, J. H., and J. Suppe (1996), Earthquake hazards of active blind-thrust faults under the central Los Angeles basin, California, *J. Geophys. Res.*, *101*(B4), 8623–8642, doi:10.1029/95JB03453.
Sliter, R. W., W. R. Normark, and C. E. Gutmacher (2005), Multichannel seismic-reflection data acquired off the coast of Southern California—Part A 1997, 1998, 1999, and 2000, *U.S. Geol. Surv. Open File Rep.*, *2005-1084*.
Sorlien, C. C., L. Seeber, K. G. Broderick, B. P. Luyendyk, M. A. Fisher, R. W. Sliter, and W. R. Normark (2013), The Palos Verdes anticlinorium along the Los Angeles, California coast: Implications for underlying thrust faulting, *Geochem. Geophys. Geosyst.*, *14*, 1866–1890, doi:10.1002/ggge.20112.
Stephenson, W. J., T. K. Rockwell, J. K. Odum, K. M. Shedlock, and D. A. Okaya (1995), Seismic reflection and geomorphic characterization of the onshore Palos Verdes fault zone, Los Angeles, California, *Bull. Seismol. Soc. Am.*, *85*(3), 943–950.
Stuiver, M., and T. F. Braziunas (1993), Sun, ocean, climate and atmospheric 14CO2: An evaluation of causal and spectral relationships, *Holocene*, *3*(4), 289–305.
Stuiver, M., P. J. Reimer, and R. W. Reimer (2014), CALIB Radiocarbon Calibration Execute Version 7.0.2, edited.
Sumner, E. J., M. I. Siti, L. C. McNeill, P. J. Talling, T. J. Henstock, R. B. Wynn, Y. S. Djajadihardja, and H. Permana (2013), Can turbidites be used to reconstruct a paleoearthquake record for the central Sumatran margin?, *Geology*, *41*(7), 763–766.
Sylvester, A. G. (1988), Strike-slip faults, *Geol. Soc. Am. Bull.*, *100*(11), 1666–1703.
ten Brink, U. S., J. Zhang, T. M. Brocher, D. A. Okaya, K. D. Klitgord, and G. S. Fuis (2000), Geophysical evidence for the evolution of the California Inner Continental Borderland as a metamorphic core complex, *J. Geophys. Res.*, *105*(B3), 5835–5857, doi:10.1029/1999JB900318.
U.S. Geological Survey and California Geological Survey (2014), Quaternary fault and fold database, edited by USGS, USGS. [Available at http://earthquakes.usgs.gov/regional/qfaults/.]
Ward, S. N., and G. Valensise (1994), The Palos Verdes terraces, California: Bathtub rings from a buried reverse fault, *J. Geophys. Res.*, *99*(B3), 4485–4494, doi:10.1029/93JB03362.
Wells, D. L., and K. J. Coppersmith (1994), New empirical relationships among magnitude, rupture length, rupture width, rupture area, and surface displacement, *Bull. Seismol. Soc. Am.*, *84*(4), 974–1002.